



Title	Electronic band structures and optical properties of LiCaAlF ₆ and LiYF ₄ crystals as potential vacuum ultraviolet materials in equilibrium and high pressure conditions
Author(s)	Luong, Viet Mui
Citation	大阪大学, 2017, 博士論文
Version Type	VoR
URL	https://doi.org/10.18910/67047
rights	
Note	

The University of Osaka Institutional Knowledge Archive : OUKA

<https://ir.library.osaka-u.ac.jp/>

The University of Osaka

Doctoral Dissertation

Electronic band structures and optical properties of LiCaAlF₆
and LiYF₄ crystals as potential vacuum ultraviolet materials
in equilibrium and high pressure conditions

真空紫外発光材料への応用に向けた LiCaAlF₆ 結晶・LiYF₄
結晶の高圧下における電子バンド構造と光学特性に関する
研究

Luong Viet Mui

June 2017

Graduate School of Science
Osaka University

Abstract

Electronic band structures and optical properties of LiCaAlF₆ and LiYF₄ crystals as potential vacuum ultraviolet materials in equilibrium and high pressure conditions

Luong Viet Mui

International Physics Course (IPC)

Department of Physics, Graduate School of Science

Vacuum ultraviolet (VUV) wavelengths have a wide range of technological applications such as lithography, sterilization, surface modification, and materials processing. The available VUV light sources include discharge tubes, gas lasers, higher-order harmonic generation, and synchrotron radiation. However, these sources are either large in size or unstable, and industry requires a new, compact, and solid-state light source with high efficiency and high output power. Several studies have also shown that wide band gap fluoride compounds can be used as VUV light sources. Aside from the wide band gap energies, fluorides with direct band gap transitions are also needed to develop solid-state light emitting devices with appreciable emission intensities. Lithium calcium hexafluoroaluminate

(LiCaAlF₆, LiCAF) and lithium yttrium tetrafluoride (LiYF₄, LiYF) are some of the fluoride materials that can be used as VUV laser host materials and short wavelength optical devices because of their high optical transmission down to the VUV region and low thermal lensing distortion. However, theoretical and experimental investigations of these fluoride crystals are still limited as of this moment. Previous calculations have underestimated the band gap energies, and experiments have not implemented different conditions such as varying pressure or sample temperature. Moreover, the optical properties of LiCAF and LiYF crystals such as absorption coefficient, refractive index, or transmission under high pressure are not yet investigated both theoretically and experimentally.

In this regard, we investigate the electronic band structures and optical properties of perfect LiCAF and LiYF crystals as potential VUV materials. Using optimized unit crystal volumes and equilibrium lattice constants, LiCAF and LYF have found to have an indirect band gap of 12.23 eV and a direct band gap of 11.09 eV, respectively. The band gap energies of these fluoride crystals are also observed to increase upon application of high pressure through uniform volume and uniaxial compressions. At a pressure of 110.10 GPa applied through uniform volume compression, the band gap of LiCAF shifts from an indirect band gap of 12.23 eV at equilibrium (0 GPa) to a direct band gap of 14.21 eV. On the other hand, LiYF crystal maintains its direct band gap of 11.9 eV under high pressure up to 50 GPa. The uniform and uniaxial

compressions under high pressure are investigated not only to modify the band gap energy but also to find out the best conditions to obtain the maximum direct band gap for these two fluorides. Based on the theoretical and experimental results, it is more effective to apply pressure along the c-axis in order to increase the LiCAF and LiYF band gap energies. The optical properties such as refractive index, extinction coefficient, absorption coefficient, and reflectivity are also investigated at different pressures based on the real and imaginary parts of the dielectric function. The transmission spectra of these two fluoride compounds are calculated and are found to be in good agreement with experimental results.

With these results, this study will lead not only to the better understanding of the fundamental physical phenomena and underlying mechanisms involving wide band gap fluoride crystals but also to the development of new optical devices in the VUV region. By applying pressure, we can modify the band gap energies of the fluorides, and the absorption coefficients and transmittances are shifted to higher energies. The findings feature a change in the electronic behavior and optical properties of the fluoride crystals with pressure. This investigation provides helpful insights toward the development of a solid-state and compact VUV light source based on LiCAF and LiYF crystals. High pressure compression can also be applied to other fluoride crystals to improve their properties toward VUV applications.

Keywords: hybrid functional, fluoride compounds, electronic band structures, optical properties, direct band gap, high pressure compression, VUV laser host materials, light-emitting diodes.

Acknowledgments

I wish to express my warm and sincere thanks my supervisors Prof. Nobuhiko Sarukura and Prof. Hiroshi Azechi for all their encouragement, advice and the opportunity to work in their laboratories.

My sincere thanks also goes to Prof. Peter Schwerdtferger, Dr. Krista G. Steenbergen for their assistance in learning how to use Vienna Ab initio Simulation Package (VASP) used in this dissertation and their expert advice in hybrid functional calculations.

I gratefully acknowledge Dr. Marilou Cadatal-Raduban, Dr. Melvin John Fernandez Empizo for very helpful discussions and improvement of my papers and dissertation. I wish to thank my colleagues for their support and encouragement, in particular, Assoc. Prof. Toshihiko Shimizu, Yuki Minami and Yasufumi Umemura.

I gratefully acknowledge the Institute for Materials Research (IMR), Tohoku University, Japan and Centre for Theoretical Chemistry and Physics (CTCP), Massey University, New Zealand for computational resources.

Last but not the least, I would like to thank my wife Fan Chih-Ying for her support and encouragement, my children Luong Minh Hi, and my parents who have always encouraged me.

During the course of my research, I have received financial support from Global 30 program, Graduate School of Science, Osaka University and Ministry of Education, Culture, Sports, Science and Technology (MEXT), Japan.

Contents

Abstract

Acknowledgments

Contents

List of figures

List of tables

List of Abbreviations

1. Purpose and motivation.....	18
2. Theoretical framework	24
2.1 Density functional theory (DFT).....	24
2.2 Generalized gradient approximation (GGA).....	27
2.3 Hybrid Perdew-Burke-Ernzerhof (PBE) functional	31
2.4 Vienna ab initio simulation package (VASP)	33
2.5 Computational methods.....	34
3. The electronic band structure and optical properties of LiCaAlF₆ crystal.....	38

3.1 Crystal structure of LiCAF crystal	39
3.2 Optimized volume of LiCAF crystal.....	41
3.3 Equilibrium structure of LiCAF crystal	42
3.3.1 Electronic band structure	42
3.3.2 Density of state	44
3.3.3 Charge density	45
3.3.4 Optical properties	47
3.3.5 Comparison of Ce:LiCAF and Ce:LiSAF crystals on solarization effect.....	50
3.4 Uniform volume compression of LiCAF crystal.....	52
3.4.1 Electronic band structure	52
3.4.2 Density of state	55
3.4.3 Pressure dependence of band gap energy and volume	
3.5 Pressure dependence of band gap energy under uniaxial compression of LiCAF crystal	58
3.6 Conclusions.....	60
Supplemental information	62
4 Uniaxial compression for LiCaAlF₆ crystal by high pressure laser-shock.....	64

4.1 Experimental setup	65
4.2 X-ray diffraction	66
4.3 Conclusions.....	69
5 The electronic band structure and optical properties of LiYF₄ crystal.....	70
5.1 Crystal structure of LiYF ₄ crystal	71
5.2 Optimized volume of LiYF ₄ crystal.....	72
5.3 Equilibrium structure of LiYF ₄ crystal.....	73
5.3.1 Electronic band structure	74
5.3.2 Density of state	75
5.3.3 Charge density	76
5.3.4 Optical properties	78
5.4 Uniform volume compression of LiYF ₄ crystal	81
5.4.1 Electronic band structure	82
5.4.2 Density of states.....	84
5.4.3 Pressure dependence of band gap energy and volume	
5.4.4 Optical properties	86
5.5 Pressure dependence of band gap energy under uniaxial compression	89
5.6 Conclusions.....	90

6 Summary	92
References	95
List of publications	110
List of Attended Scientific Meeting	114

List of figures

1.1 The transmission of colquiriite-type fluoride single crystals in the vacuum UV region.....	20
1.2 The transmission spectrum of LiYF ₄ single crystal	21
1.3 The direct and indirect band gap energy diagrams	22
2.1 A flow chart of the iteration scheme.....	27
2.2 Theoretical versus experimental band gaps by different methods	33
3.1 (a) Colquiriite-type structure and (b) first Brilloiu zone of hexagonal unit cell of the LiCAF crystal	39
3.2 Optimized volumes of the LiCAF crystal. The curve is fitted using the Murnaghan equation of state.....	41
3.3 Simulated electronic band structure diagram of LiCAF crystal having indirect band gaps of 12.23 eV.....	43
3.4 The total and partial density of states of perfect LiCAF crystal.....	45
3.5 The charge density distributions of LiCAF crystal in the different planes (a) 001 plane, 1.45 Å from the origin perpendicular to the z-axis, (b) 010 plane, 2.80 Å from the origin perpendicular to the y-axis and (c) 100 plane, 2.85 Å from the origin perpendicular to the x-axis	46
3.6 The real and imaginary parts of dielectric function of LiCAF crystal	48
3.7 The refractive index and absorption coefficient of LiCAF crystal.....	49
3.8 Electronic band structure and density of states of LiSrAlF ₆ crystal	50

3.9 Schematic diagram of ESA and solarization effect in Ce:LiCAF and Ce:LiSAF crystals.....	51
3.10 Simulated electronic band structure diagrams of the LiCAF crystal at (a) 0, (b) 16.32, (c) 48.26 GPa, and (d) 110.10 GPa applied pressure. The band gap is close to becoming direct at 110.10 GPa applied pressure	53
3.11 Simulated electronic band structure diagrams of the LiCAF crystal at (a) 0, (b) 16.32, (c) 48.26 GPa, and (d) 110.10 GPa applied pressure. The band gap shift to direct at 110.10 GPa pressure, assuming picosecond experimental time scales.....	54
3.12 Total and partial density of states of the LiCAF crystal at (a) 0 and 110.10 GPa applied through uniform volume compression for the case when (b) ions are not allowed to relax and (c) ions relax.....	56
3.13 (a) Unit crystal volume and (b) band gap energy of the LiCAF crystal at different pressures applied through uniform volume compression. The band gap increases monotonically with pressure up to 50 GPa	57
3.14 Optimized (a) a and (b) c lattice constants of the LiCAF crystal.	59
3.15 (a) Lattice constant compression and (b) band gap energy of the LiCAF crystal at different pressures applied through uniaxial compression. Maximum band gap energies of 12.52 and 12.63 eV are achieved with uniaxial compression along the a-axis and c-axis, respectively using 7.6 GPa applied pressure	60
4.1 The experimental set up for uniaxial compression of LiCAF crystal by laser-shock	66
4.2 XRD patterns of the LiCAF crystal with laser-shock compression along the a-axis at different delay times of (a) 0, (b) 5.90, (c) 12.1, (d) 16.3, (e) 20.5, (f) 21.7, and (g) 29.3 ns. h) Laue XRD simulation used to obtain compression ratios.....	67

4.3 XRD patterns of the LiCAF crystal after laser-shock compression along the c-axis at different delay times of (a) 0, (b) 6.65, (c) 11.9, (d) 15.5, (e) 18.8, (f) 23.1, and (g) 31.1 ns. (h) Laue XRD simulation used to obtain the compression ratios.....	67
4.4 Lattice constant compression of the LiCAF crystal obtained at different delay times after the laser shock	68
5.1 (a) Scheelite-type structure and (b) first Brillouin zone of tetragonal unit cell of the LiYF ₄ crystal	71
5.2 Optimized volumes of the LiYF crystal. The curve is fitted using the Murnaghan equation of state.....	73
5.3 Simulated electronic band structure diagram of the LiYF ₄ crystal having direct band gap of 11.09 eV at gamma point.....	74
5.4 Total and partial DOS of the LiYF ₄ crystal. The red, blue, and green lines represent different orbitals in each atom.....	76
5.5 The charge density contours in the different planes (a) 001 plane, 2.20 Å from the origin perpendicular to the z-axis, (b) 010 plane, 1.30 Å from the origin perpendicular to the y-axis and (c) 100 plane, 0.00 Å from the origin perpendicular to the x-axis	78
5.6 The real part (a) and imaginary parts of dielectric function of the LiYF ₄ crystal	79
5.7 The optical properties such as refractive index (a), absorption coefficient (b), transmission (red) and reflectivity (blue) (c) of the LiYF ₄ crystal	81
5.8 The simulated electronic band structure diagrams of LiYF ₄ crystal at (a) 10, (b) 30 and (c) 50 GPa. LiYF crystal maintains direct band gap under high pressure up to 50 GPa.....	82

5.9 The total and partial density of states of LiYF ₄ crystal at (a) 10, (b) 30 and (c) 50 GPa, respectively	83
5.10 (a) Optimized crystal volume and (b) lattice constants of the LiYF ₄ crystal at different pressures. The crystal volume and lattice constants decreases monotonically since the pressures are applied through uniform volume compression	85
5.11 Band gap energy of the LiYF ₄ crystal at different pressures. LiYF ₄ has a band gap energy which gradually increases up to 30 GPa and stays almost the same up to 50 GPa.	86
5.12 The real part (a) and imaginary parts of dielectric function of the LiYF ₄ crystal at different pressure.....	87
5.13 The refractive index (a) and absorption coefficient (b) of the LiYF ₄ crystal at different pressure	88
5.14 The transmission spectrum of LiYF ₄ crystal at different pressure	88
5.15 Simulated (a) lattice constant compression and (b) band gap energy of the LiYF crystal at different pressures applied through uniaxial compression	

List of tables

3.1 The atomic position of LiCAF atoms	40
3.2 The reciprocal lattice vectors of highly symmetric points in the first Brillouin zone of hexagonal for $c>a$	40
3.3 Comparison of lattice constants, crystal volume, bulk modulus, and band gap energy for LiCAF crystal from previous calculations and experimental results. The values inside the parentheses indicate the percent differences from the experimental results	44
5.1 The atomic positions of LiYF ₄ crystal	72
5.2 The symmetry points of the first Brillouin zone for tetragonal structure	
5.3 Comparison of lattice constants, crystal volume, bulk modulus, and band gap energy for LiYF crystal from previous calculations and experimental results. The values inside the parentheses indicate the percent differences from the experimental results	75
S3.1 Lattice constants, crystal volumes, and band gap energies of the LiCAF at different pressures applied through uniform volume compression. The values inside the parentheses indicate the percent differences compared to the equilibrium value (0 GPa)	62
S3.2 Lattice constants, crystal volumes, and band gap energies of the LiCAF at different pressures applied through uniaxial compression along the a-axis. The values inside the parentheses indicate the percent differences compared to the equilibrium value (0 GPa)	62

S3.3 Lattice constants, crystal volumes, and band gap energies of the LiCAF at different pressures applied through uniaxial compression along the c-axis. The values inside the parentheses indicate the percent differences compared to the equilibrium value (0 GPa)63

List of abbreviations and symbols

DFT	Density functional theory
PBE	Perdew-Burke-Ernzerhof
HF	Hartree-Fock
H	Hamiltonian
E	Energy
Ψ	Wave function
LiCaAlF_6	Lithium calcium hexafluoroaluminate
LiYF_4	Lithium yttrium tetrafluoride
UV	Ultraviolet
VUV	Vacuum ultraviolet
DOS	The density of states
TDOS	Total density of state
PDOS	Partial density of state
E_g	Band gap energy
V	Volume

B	Bulk modulus
K	Compressibility
ϵ_1	Real part of dielectric function
ϵ_2	Imaginary part of dielectric function
n	Refractive index
n_o	Ordinary component of refractive index
n_e	Extra-ordinary component of refractive index
k	Extinction coefficient
α	Absorption coefficient
R	Reflectivity
T	Transmission
LED	Light emitting diodes

Papers arising out of this dissertation

1. **Mui Viet Luong**, Melvin John F. Empizo, et.al, “*Direct band gap tunability of LiYF₄ crystal by uniaxial and uniform volume compression*”, preparation in progress.
2. Toshihiko Shimizu, **Mui Viet Luong**, et. al., “*High pressure band gap modification of LiCaAlF₆*”, Applied Physics Letter **110**. 141902 (2017).
3. **Mui Viet Luong**, Melvin John F. Empizo, et. al., “*First-principles calculations of electronic and optical properties of LiCaAlF₆ and LiSrAlF₆ crystals as VUV to UV solid-state laser materials*”, Optical Materials **65**, 15 - 20 (2017).
4. **Mui Viet Luong**, Marilou Cadatal-Raduban, et. al., “*Comparison of the electronic band structures of LiCaAlF₆ and LiSrAlF₆ ultraviolet laser host media from ab initio calculations*” Japanese Journal of Applied Physics **54**, 122602 (2015).

Chapter 1

Purpose and motivation

Vacuum ultraviolet (VUV) wavelengths are expected to have a wide range of applications for lithography, sterilization, surface modification, and materials sciences to name a few. Discharge tubes, gas lasers, high-order harmonic generation, and synchrotron radiation are some of the available light sources for VUV. These present sources, however, are very huge or unstable, therefore a new, compact, and solid-state light source is needed with high efficiency and high output power. Some of the possible solid-state VUV media are the wide band gap fluoride materials. Lithium calcium hexafluoroaluminate (LiCaAlF_6 , LiCAF) and lithium yttrium tetrafluoride (LiYF_4 , LiYF) are among the fluoride compounds that can be used as a VUV scintillator, lens, or host material because of its high optical transmission down to the VUV region and low thermal lensing distortion [1-4]. In addition, fluoride compounds with direct band gap transitions are needed in order to develop short wavelength solid-state light emitting devices with appreciable

emission intensities [5]. However, theoretical and experimental investigations of this fluoride crystals are still limited [6-10]. For example, previous calculations have underestimated the band gap energies [11-13], and the experiments have not implemented different conditions such as varying pressure or temperature. Moreover, the optical properties of LiCAF and LiYF crystals such as absorption coefficient, refractive index, or transmission under high pressure are not investigated both theoretically and experimentally.

V. W. Viebahn et al. first presented the LiCAF structure in 1971 and suggested its use as a laser host material [14]. In 1988, a laser made up of chromium-doped LiCAF (Cr^{3+} :LiCAF) had a slope efficiency of 67 % and a peak emission wavelength at 760 nm [15]. M. A. Dubinskii et al. then pioneered the active investigation of LiCAF crystals as ultraviolet (UV) laser host materials over the past 20 years. In 1993, they identified cerium-doped LiCAF (Ce^{3+} :LiCAF) as an efficient and convenient solid-state UV laser media. LiCAF and other fluoride compounds doped with Ce^{3+} showed a broad of emission from 275 nm to 335 nm [16,17]. Some common growth techniques such as Czochralski and micro-pulling down methods were eventually improved to prepare high-quality and large Ce^{3+} :LiCAF crystals [3,18,19]. Compared to a similar compound, lithium strontium hexafluoroaluminate (LiSrAlF_6 , LiSAF), LiCAF has a reduced excited state absorption (ESA) and an almost negligible solarization when doped with rare-earth ions such as Ce^{3+} [20]. Strong VUV

fluorescence were then reported recently for erbium (Er^{3+}), thulium (Tm^{3+}), and neodymium (Nd^{3+})-doped LiCAF crystals [21-24].

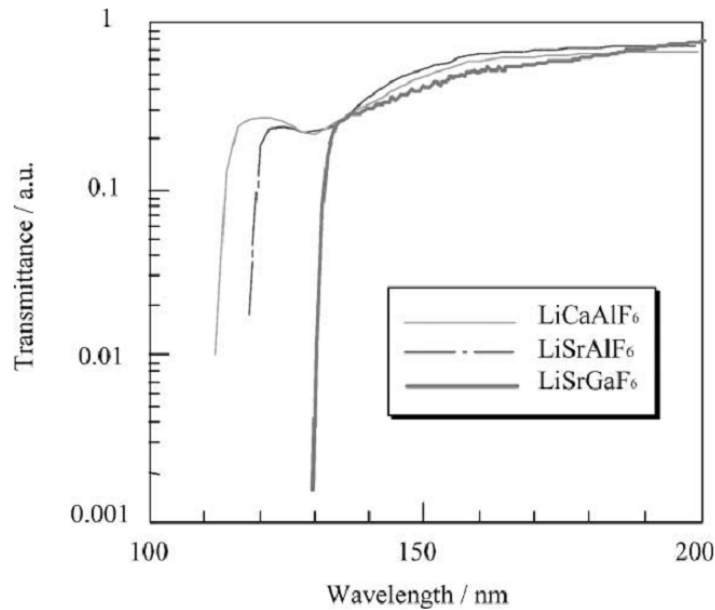


Fig 1.1 The transmission of colquiriite-type fluoride single crystals in the vacuum UV region.

On the other hand, the first structural data of LiYF_4 is obtained by Thomas et al. [25] in 1961, just one year after demonstration of the first laser. The host crystal LiYF_4 is an incongruently melting compound with a scheelite structure. This compound is suitable for the introduction of trivalent rare-earth ions, which serve as a substitute for the Y^{3+} ion. LiYF_4 crystals doped with rare-earth ions have been proven to be efficient tunable all-solid-state lasing media that cover varied wavelength regions [26-29]. Nd^{3+} -doped LiYF_4 crystal has been applied in infrared (IR) solid-state lasers with emissions ranging from 1.047 to 1.053 μm . With the use of an ultraviolet (UV) laser crystal $\text{Ce}^{3+}:\text{LiYF}_4$, a tunable laser output ranging from 306 to 330 nm can be

achieved. In addition to being an excellent laser medium, pure LiYF₄ crystal can also be a valuable window material. The fluoride crystal may be used as a suitable optical material for lenses and other optical components. Due to its importance as host materials for laser applications, undoped or doped LiYF₄ was extensively studied during the last years. LiYF₄ crystal is one of the few fluoride compounds which is direct band gap originally. Based on this property, this crystal can be used not only for laser host material but also for light-emitting diode and optical devices in vacuum ultraviolet and ultraviolet regions.

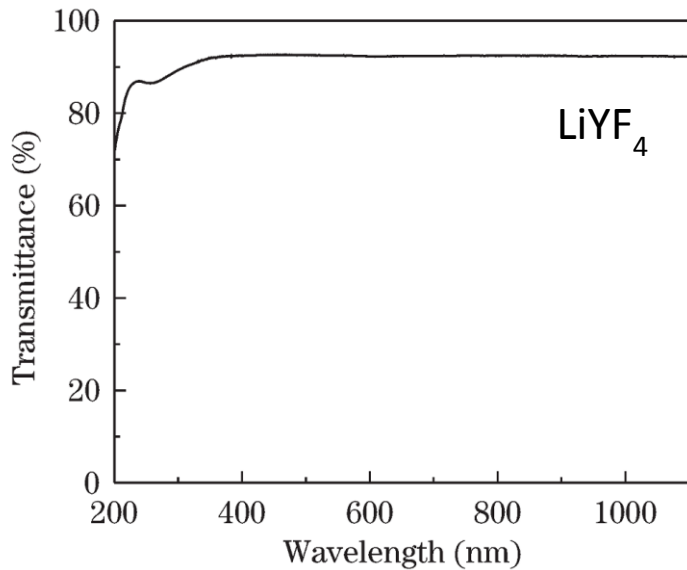


Fig 1.2 The transmission spectrum of LiYF₄ single crystal

Since the absorption or fluorescence wavelength is dependent on the band gap energy, wide band gap fluoride materials are preferred for the development of short wavelength optical devices. In addition, direct band gap transition is desirable for optical devices with strong emission. Band gap

engineering is generally achieved using lattice distortion by controlling the composition of the material or by doping the material with impurities. These methods often lead to completely different material properties and growth procedures. On the other hand, material compression under high pressure is remarkable in changing the lattice parameters while keeping the composition constant. A silicon-germanium (Si-Ge) semiconductor superlattice has been predicted to have an indirect to direct band gap transition in 1987 [30]. Moreover, band gap transition has also been reported for lithium fluoride (LiF) under high pressure [31]. By applying a hydrostatic pressure of 70 GPa, the LiF compound transforms from direct band gap to indirect band gap insulator with changes on its optical properties.

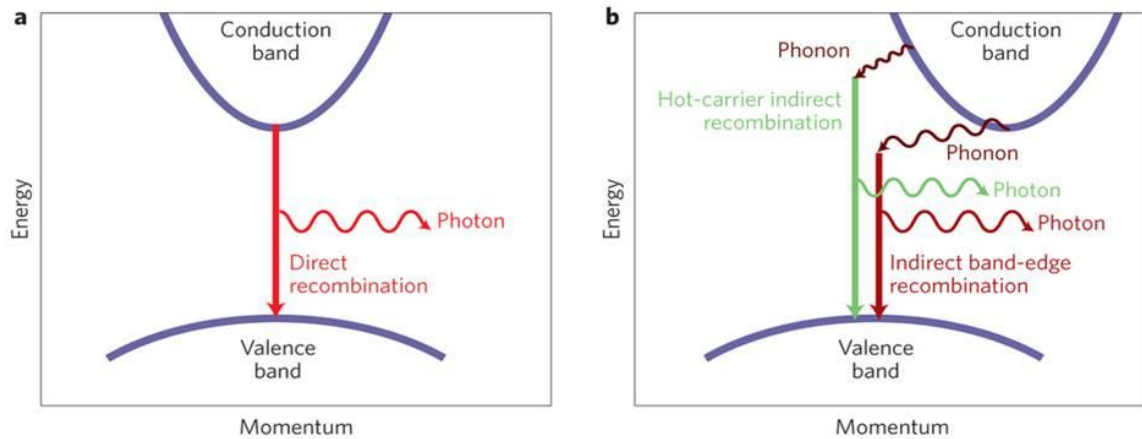


Fig 1. 3 : The direct and indirect band gap energy diagrams

Exploring the possibilities of improving the properties of potential VUV fluoride materials, we investigate the effects of high pressure applied through uniform volume and uniaxial compression on the electronic band structure of perfect LiCAF and LiYF crystals by hybrid functional. First-principles

calculations are performed within the framework of density functional theory (DFT) employing amount of the exact exchange. The hybrid density functional studies of band gaps have demonstrated that including some HF exchange improves results dramatically. A laser-shock compression of a pure LiCAF crystal is also demonstrated to experimentally verify the numerical results of the lattice compressions. With an increase and a transition of band gap energy for LiCAF crystal while LiYF crystal maintains the direct band gap under high pressure, our findings provide helpful insights for the further development of this fluoride compounds as a VUV laser host material considering rare-earth ion doping or high pressure application.

The outline of this dissertation is as follows. Chapter 2 introduces the density functional theory as well as the methodology used. Chapter 3 is a study on the electronic band structure and optical properties of LiCAF crystal at the equilibrium and high pressure application. The experiment of LiCAF crystal under uniaxial compression by laser-shock are presented in chapter 4. Similarity to chapter 3, chapter 5 presents the electronic band structure and optical properties of LiYF crystal. Conclusions of the dissertation are presented in chapter 6.

Chapter 2

Theoretical framework

Quantum mechanics was developed in the early part of the twentieth century to solve problems which couldn't be explained by classical mechanics. To model the electronic structure of materials using quantum mechanics, Schrödinger's equation must be solved; however in nearly all cases we can't solve Schrödinger equation exactly. This chapter outlines the various approximations used and the mechanics of solving within these approximations, as well as some of the general physics used in this dissertation.

1. Density functional theory

Since Dirac's well-known quote more than 80 years have passed and his statement is still as true as at his time: "For any dynamical system with a classical analogue, a state for which the classical description is valid as an approximation is represented in quantum mechanics by a wave packet, all the coordinates and momenta having approximate numerical values ...

Schrodinger's wave equation fixes how such a wave packet varies with time, so in order that the classical description may remain valid, the wave packet should remain a wave packet and should move according to the laws of classical dynamics." [32-33]. Nevertheless with the advent of computer assisted calculations, several numerical techniques for solving the many-particle Schrödinger equation became feasible [34]. Density functional theory (DFT) is one of the most efficient methods to solve the Schrödinger equation, as it maps the complicated interacting many-body problem exactly to an equivalent non-interacting single-particle one [36-37].

The impact of DFT for the theoretical investigation of complex molecules and solids manifested itself in the Nobel Prize for Walter Kohn in 1998. In his Nobel lecture, he highlighted two of the important contributions DFT made to the field of many-body quantum physics [38-41]. On the one hand DFT simplified the understanding of these systems by reducing the complexity from the multiple-particle wave-function with $3N$ independent coordinates, where N is the number of electrons, to the density $n(r)$ which can be much easier visualized, analyzed, and hence comprehended. This reduction in complexity on the other hand made numerical calculations possible. Numerical DFT calculations grew significantly in popularity in the 1990s once the balance between accuracy and computational cost was demonstrated [42-44]. Nowadays, DFT is successfully used to investigate materials properties from first principles.

Schrodinger equation is Eq. 2.2, where $e^2 = \hbar = 1$, the H is the Hamiltonian of the system, ψ is the wave function and \mathbf{r}_i denotes the position vector of electron.

$$H \Psi (r_1, r_2, \dots, r_n) = E \Psi (r_1, r_2, \dots, r_n) \quad 2.1$$

this can be written explicitly as

$$\left\{ \sum_{i=1}^n -\frac{1}{2} \nabla_i^2 + \sum_{i=1}^n v_{ext}(r_i) + \sum_{i < j}^n v_{ee}(r_i, r_j) + \sum_{i=1}^n v_{XC}(r_i) \right\} \Psi (r_1, r_2, \dots, r_n) = E \Psi (r_1, r_2, \dots, r_n) \quad 2.2$$

The first term of left in the equation is kinetic energy of electrons, the second term v_{ext} is external potential by atom and the v_{ee} is electron-electron interaction, and the v_{XC} is exchange-correlation potential due to the Pauli's exclusion principle and correlation energy which is remaining unknown piece of energy, n is the number density of electron which is larger than Avogadro's number in solid. Solving the Schrodinger equation directly is hard because, it is too complicate to calculate, so, we need a suitable approximation which is called density functional theory.

The mechanism of DFT to solve Kohn-Sham equation is represented in the Fig 2.1. At first, an initial guess for the electron density is assumed, which is required for the calculation of $v_{eff}(r)$, the diagonalization of the Kohn-Sham equations, and the subsequent evaluation of $\rho(r)$ along with E_{total} . As long as

the convergence criterion is not fulfilled, the numerical procedure is continued with the last $\rho(r)$ instead of the initial guess. When the criterion is satisfied, various output quantities are computed.

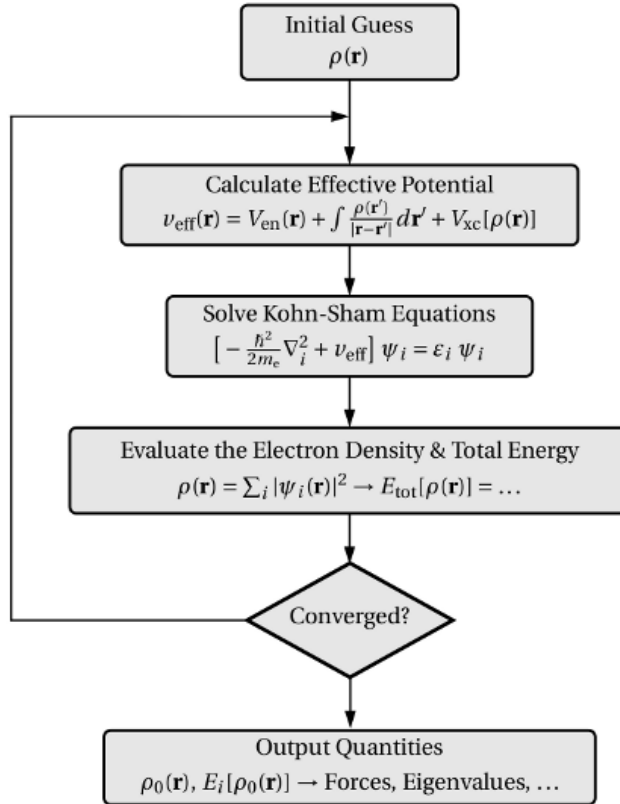


Fig. 2.1 A flow chart of the iteration scheme.

2. Generalized gradient approximation (GGA)

The idea of constructing a functional that is not as computationally demanding as fully non local functionals and yet possesses a potential that does not diverge for exponentially decaying densities would be groundbreaking. One of the first suggestions into expanding the exchange

correlation parameter in function of the magnitude of the gradient of the density was given in the original paper of Kohn and Sham [45] and it was referred to as a gradient expansion approximation (GEA). The insertion of gradient-dependent functionals into the local density approximation of the exchange correlation parameter was first thought to be very attractive for applications but unfortunately most gradient expansion approximations did not lead to consistent improvements over the LSDA. Such failure could be explained by the fact that the gradient in real materials is so large that a given gradient expansion would break down. Indeed, the major drawbacks of the GEA were that its corresponding exchange correlation hole was not physical, nor did it satisfy the normalization conditions of the exchange and correlation holes and the negativity state of the exchange hole [46,47]. By eliminating the spurious long-range term of the second order expansion of the GEA exchange-correlation hole, generalized gradient approximations [48-50] (GGAs) were created and their corresponding exchange correlation energy were approximated by:

$$E_{xc}^{GGA} [n^\uparrow, n^\downarrow] = \int d^3r n(\vec{r}) \varepsilon_{xc} (n^\uparrow, n^\downarrow, |\nabla n^\uparrow|, |\nabla n^\downarrow| \dots) \quad 2.3$$

GGA functionals have recently become quite popular in condensed matter physics. As a general trend, GGAs yield more accurate atomization energies total energies and barriers to chemical reactions than LSDA [51-53]. Furthermore GGAs can also correct the underestimation of bulk constant previously computed by LSDA. One of the arguably most crucial improvements

of the GGAs over LSDA is the prediction of the correct ferromagnetism configuration of bcc ground state metallic iron [54]. However, except for the case of Hydrogen, GGA bond lengths computations are not better to corresponding LSDA calculations for arbitrarily chosen molecules [55, 56]. Even though some GGAs provide some improvements over the LSDA, one should keep a realistic perspective of the predictive power of the GGAs and further understanding on the properties of each GGA functional is therefore required. One of the first serious attempts into writing a gradient functional that would be subjected to further improvements in the near future was performed by Perdew and Wang in 1986 (PW86) [48]. New physical insight was brought upon the exchange and correlation parameter when, $E_{xc}^{GGA} [n^\uparrow, n^\downarrow]$ was rewritten as [57]:

$$E_{xc}^{GGA} [n^\uparrow, n^\downarrow] = \int d^3r \ \varepsilon_x^{unpol}(n) F_{xc}^{unpol}[s(\vec{r}), r_s(\vec{r})] \quad 2.4$$

here $\varepsilon_x^{unpol}(n) = -\frac{3}{4} \left(\frac{3}{\pi} n(\vec{r}) \right)^{\frac{1}{3}}$ is the exchange energy in an unpolarized system previously computed from the LDA formalism and F_{xc}^{unpol} is the dimensionless enhancement factor over local exchange. In order to distinguish a GGA that would offer a consistent improvement over the previous LSDA, several authors decided to plot the GGA dimensionless enhancement factor F_x^{GGA} in function of reduced density gradient [57, 58]:

$$s(\vec{r}) = \frac{|\nabla n(\vec{r})|}{2k_F n(\vec{r})} \quad 2.5$$

for various values of Wigner-Seitz radius $r_s(\vec{r}) = \left(\frac{3}{4\pi n(\vec{r})}\right)^{1/3}$

Here, $k_F = (3\pi^2 n(\vec{r}))^{1/3}$ is the local Fermi wavevector

A non-monotonic behavior from various famous functionals such as Becke [49], Perdew and Wang (PW91) and the famous Perdew-Burke-Enzherof (PBE) [59] is observed after plotting the exchange part of the enhancement factor F_x in function of the reduced density gradient $s(\vec{r})$. Huge discrepancies among the functionals appear for large regions of $s(\vec{r})$ and such differences might be explained by the inaptitude of well describing regions that contain large gradient by the density gradient expansion. Although some widely used gradient formalism such as the PBEGGA and PW91 predict several correct physical properties, one cannot guarantee their absolute superiority in the entire condensed matter field.

As one would have expected, even though the correlation energy is a lot smaller than the exchange energy, rewriting the correlation parameter as a functional is quite complex. In generalized gradient approximations, some interesting works have been done on estimating the correlation [52, 59, 60] parameter but further improvements are still required in this area. Unfortunately, regardless of how precise these gradient functionals are constructed, DFT calculations are still not exact solutions of the full Schrodinger equation. Even though the true ground state energy of a given system can be well approximated by pure DFT, one can still

not compute excited state energies. In addition to the non-time dependence of DFT, there exist important situations for which DFT computations yield unphysical results. The underestimation of band gaps in semiconductors and insulators and the inaccurate weak Van der Waals attractions are one of the main disadvantages in the density functional formalism. Hence, instead of attacking the many-body problem from a pure electron density perspective, one might reconsider computing wave functions that would converge to an exact solution of the Schrodinger equation.

3. Perdew-Burke-Ernzerhof (PBE) hybrid functional

Density-functional-related methods have impressively proven their computational relevance during the last decades. Density-functional theory (DFT) is now established in computational materials science as well as in quantum chemistry. Although reasonably successful in the description of the energetics, the local-density approximation and gradient corrected functionals have several severe shortcomings. Moreover, present local- and semilocal-density functionals severely underestimate band gaps. Although DFT, as a ground-state theory, is per se not capable to yield a description of excited states, the underestimation of band gaps imposes a severe problem if density-functional theory is applied to the modeling of semiconductors and insulators.

In hybrid functionals the otherwise semilocal-density functional is modified by adding a fraction of the exact exchange energy. Hybrid-functional

methods represent a sensible compromise between two simple mean-field methods [DFT and Hartree–Focks (HF)], and they often yield results that are astonishingly close to state of the art many-body methods (configuration interaction, perturbation theory). The formation energies of small molecules are, for instance, in substantially better agreement with experiment than with local functionals, and band gaps and the band structures agree often reasonably well with experiment.

We therefore use the hybrid functional which performs the exact exchange mixing only for short range interactions in both HF and DFT. This allows the DFT exchange hole to become delocalized among the near neighbors of a reference point, but not beyond. As a starting point, we use the PBE0 hybrid functional [61-63], which is based on the Perdew-Burke-Ernzerhof (PBE) exchange-correlation functional [59]. PBE0 assumes the following form for the exchange-correlation energy:

$$E_{XC}^{PBE0} = \alpha E_x^{HF} + (1 - \alpha) E_X^{PBE} + E_c^{PBE} \quad 2.6$$

where the mixing coefficient $\alpha=0.25$ is determined by perturbation theory [17]. We now focus on the expression for the exchange energy

$$E_X^{PBE0} = \alpha E_x^{HF} + (1 - \alpha) E_X^{PBE} \quad 2.7$$

Hence, Exchange correlation functionals that admix a certain amount of Fock exchange to (a part of) a local or semi-local density functional [64].

- Present a definite improvement over the (semi)-local density functional description of the properties of molecular systems.
- Some hybrid functionals yield an improved description of structural, electronic, and thermo-chemical properties of small/medium gap solid state systems.

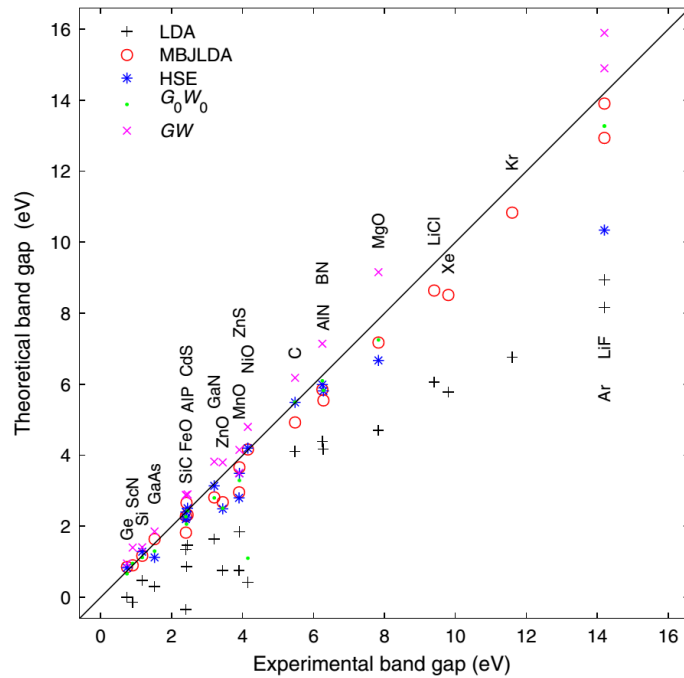


Fig. 2.2 Theoretical versus experimental band gaps by different methods

4. Vienna ab-initio simulation package (VASP)

VASP is a complex package for performing ab-initio quantum-mechanical molecular dynamics (MD) simulations using pseudopotentials or the projector-augmented wave method and a plane wave basis set. The approach implemented in VASP is based on the (finite-temperature) local-

density approximation with the free energy as variational quantity and an exact evaluation of the instantaneous electronic ground state at each MD time step. VASP uses efficient matrix diagonalisation schemes and an efficient Pulay/Broyden charge density mixing. These techniques avoid all problems possibly occurring in the original Car-Parrinello method, which is based on the simultaneous integration of electronic and ionic equations of motion. The interaction between ions and electrons is described by ultra-soft Vanderbilt pseudopotentials (US-PP) or by the projector-augmented wave (PAW) method. US-PP (and the PAW method) allow for a considerable reduction of the number of plane-waves per atom for transition metals and first row elements. Forces and the full stress tensor can be calculated with VASP and used to relax atoms into their instantaneous ground-state.

5. Computational methods

Based on the experimental data of lattice constants and atomic positions, the total energy of system are calculated for both LiCAF and LiYF crytals. And then the unit cell volume is initially optimized by using the Murnaghan equation of state to fit the curve of the total energy as a function of volume [65]. The lattice constants are then obtained from the optimized volumes to compute for the electronic band structures and optical properties of fluoride compounds. For the band structure and density of states (DOS) diagrams, the k-points are chosen following the Brillouin zone with symmetry points. All valence band

maxima of the resulting diagrams are also shifted to zero. For the optical properties, the complex dielectric function forms the basis of the refractive index, absorption coefficient, and optical transmittance. The complex dielectric function represents the linear response of the system to an external electromagnetic field with a small wave vector. The complex shift in the Kramers-Kronig transformation is 0.1 which is a perfectly acceptable value. The complex dielectric function can be expressed as

$$\varepsilon(\omega) = \varepsilon_1(\omega) + i\varepsilon_2(\omega) \quad 2.8$$

where the $\varepsilon_1(\omega)$ and $\varepsilon_2(\omega)$ are the real and imaginary parts of the dielectric function, respectively. The imaginary part $\varepsilon_2(\omega)$ is given by [66-68]:

$$\varepsilon_2(\omega) = \left(\frac{4\pi^2 e^2}{m^2 \omega^2}\right) \sum \int \langle i|M|j \rangle^2 f_i (1 - f_j) \times \delta(E_f - E_i - \omega) d^3 k \quad 2.9$$

where M is the dipole matrix, i and j are the initial and final states of electron, respectively. f_i is the Fermi distribution for the i^{th} state, and E_i is the energy of electron in the i^{th} state. The Kramers-Kronig relation is used to extract the real part from the imaginary part of the dielectric function [69]. Using the Kramers-Kronig relation, the real part $\varepsilon_1(\omega)$ is given by:

$$\varepsilon_1(\omega) = 1 + \frac{2}{\pi} P \int_0^\infty \frac{\omega' \varepsilon_2(\omega') d\omega'}{(\omega'^2 - \omega^2)} \quad 2.10$$

where P is the principal value of the integral. From the components of the dielectric function, the refractive index (n), absorption (α), and optical transmittance (T) can subsequently obtained from Equations 4 to 6, respectively [70, 71].

$$n(\omega) = \left[\frac{\sqrt{\varepsilon_1^2(\omega) + \varepsilon_2^2(\omega)} + \varepsilon_1(\omega)}{2} \right]^{1/2} \quad 2.11$$

$$\alpha(\omega) = \frac{2\sqrt{2}\pi f \left[\sqrt{\varepsilon_1^2(\omega) + \varepsilon_2^2(\omega)} - \varepsilon_1(\omega) \right]^{1/2}}{c} \quad 2.12$$

$$r = \frac{(n-1)^2 + k^2}{(n+1)^2 + k^2} \quad 2.13$$

where f is the frequency and k is the extinction coefficient given by the following expression:

$$k(\omega) = \left[\frac{\sqrt{\varepsilon_1^2(\omega) + \varepsilon_2^2(\omega)} - \varepsilon_1(\omega)}{2} \right]^{1/2} \quad 2.14$$

Based on the reflectivity R , the optical transmittance (T) can be calculated by:

$$T = 1 - A - R \quad 2.15$$

In this calculations of the optical properties, the local field effects are neglected in the hybrid functional approximation because we calculated for perfect fluoride compounds that mean there is no microscopic changes of the cell periodic potential, whereas the changes of exchange correlation potential are taken into account. For the optical properties, the excitonic effects play important because of Coulomb interaction between electron and hole in the conduction and valence bands, respectively. This excitonic effects is approximating within hybrid functional, GW (Green's function and the screened Coulomb interaction) routine is also performed to get better

approximations of excitonic effects for both fluorides in the equilibrium and high pressure conditions.

The effects of high pressure on the material properties are also investigated at different pressures. Different amounts of pressures are applied on the LiCAF crystal through uniform volume compression by reducing the lattice constants at the same percentage. For LiYF crystal, the Pulay stress is applied as the external pressure to compress uniformly [72]. The atomic positions and lattice constants are optimized after applying pressure, and the pressure dependence of the crystal volume, electronic band structure, and optical properties is likewise studied.

In this works, various amounts of exact exchange were initially tested, leading to the optimized values of 35% and 25% exact exchanges for LiCAF and LiYF crystals, respectively which yielded a band gap energies close to the experimental references.

Chapter 3

The electronic band structure and optical properties of LiCaAlF₆ crystal

Lithium calcium hexafluoroaluminate (LiCaAlF₆, LiCAF) crystal is widely used as vacuum ultraviolet (VUV) and ultraviolet (UV) laser host medium [21-24]. This fluoride material can be stimulated by the fourth harmonics of a Nd:YAG laser, i.e. 266 nm. When doped with trivalent cerium (Ce³⁺, Ce), the crystal becomes attractive UV solid-state laser host with a central emission wavelength of 290 nm and with a practical tuning range from 288 to 315 nm. The slope efficiencies of Ce:LiCAF has also been reported to reach as high as 39 %. The broad gain-bandwidth of the crystal in the UV region has made it appealing for ultrashort pulse generation and amplification. Aside from being a laser material, LiCAF can be used as a lens in VUV photolithography because of its optical transmission and low thermal lensing distortion. The absorption edge of LiCAF is measured to be 112 nm. The PBE exchange-correlation functional employing 35% exact exchange is used within

the framework of DFT to calculate electronic band structures, density of states (DOS), and band gap energies. Optical properties such as dielectric functions, refractive indices, and absorption coefficients are also obtained for this fluoride crystal at equilibrium and high pressure compression.

1. Crystal structure of LiCaAlF_6 crystal

LiCAF is colquiriite-type fluoride with a hexagonal crystal structure belonging to the $\text{P}-31\text{c}$ space group (group number 163). It is optically uniaxial crystal with two formula units per unit cell. Six fluorine (F) atoms surround a lithium (Li), calcium (Ca), or aluminum (Al) atom. Each Li, Ca, and Al cation occupies a deformed octahedral site as shown in Fig. 3. 1 (a). This structure is also described by an alternative stacking of metallic and fluorine atom layers parallel to c-axis [73-75]. The fraction coordinates of the representative atoms in the unit cell are shown in table 3. 1

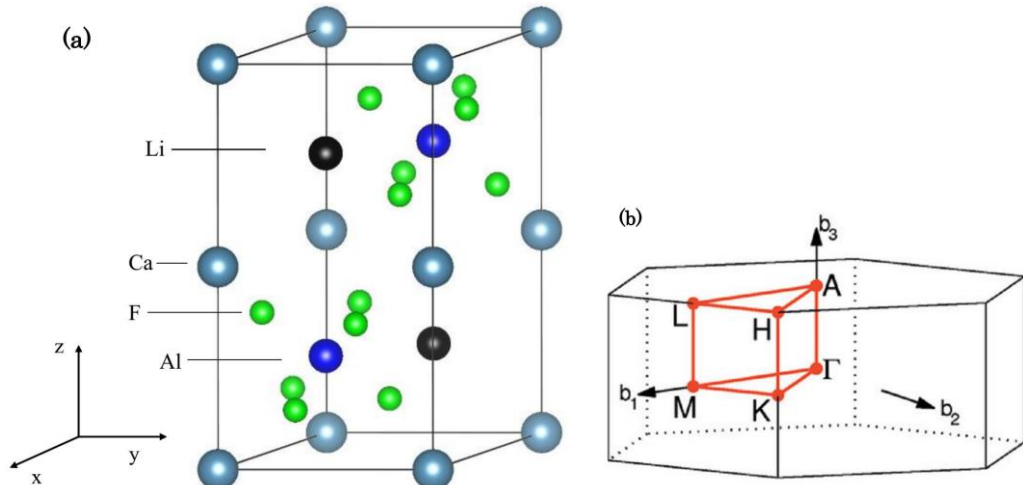


Fig. 3. 1 (a) Colquiriite-type structure and (b) first Brillouin zone of hexagonal unit cell of the LiCAF crystal.

Table 3. 1: the atomic position of LiCAF atoms

	x	y	z
Li	1/3	2/3	1/4
Ca	0	0	0
Al	2/3	1/3	1/4
F	0.3769	0.0312	0.1435

In order to generate the charge density and wave function for the first run, a 3x3x1 Monkhorst-Pack k-point grid was utilized. For the band structure and DOS diagrams, the k-points were chosen following the Brillouin zone in Fig. 1(b) with the symmetry points shown in table 3. 2 [76]. The path of k point for band structures calculation is followed: $\Gamma \rightarrow M \rightarrow K \rightarrow A \rightarrow L \rightarrow H$ with 10 k points per segment [77].

Table 3. 2: The reciprocal lattice vectors of highly symmetric points in the first Brillouin zone of hexagonal

Γ	0	0	0
M	1/2	0	0
K	1/3	1/3	0
A	0	0	1/2
L	1/2	0	1/2
H	1/3	1/3	1/2

2. Optimized volume of LiCaAlF_6 crystal

Figure 3. 2 shows the total energy as a function of the LiCAF crystal volume. The total energy as a function of the unit cell volume is expressed in terms of the Murnaghan equation of state. Table 3. 3 shows the optimized crystal volumes and the a and c lattice constants of fluoride material. LiCAF has an optimized volume of 209.55 \AA^3 with corresponding lattice constants of $4.99 (a)$ and $9.66 \text{ \AA} (c)$.

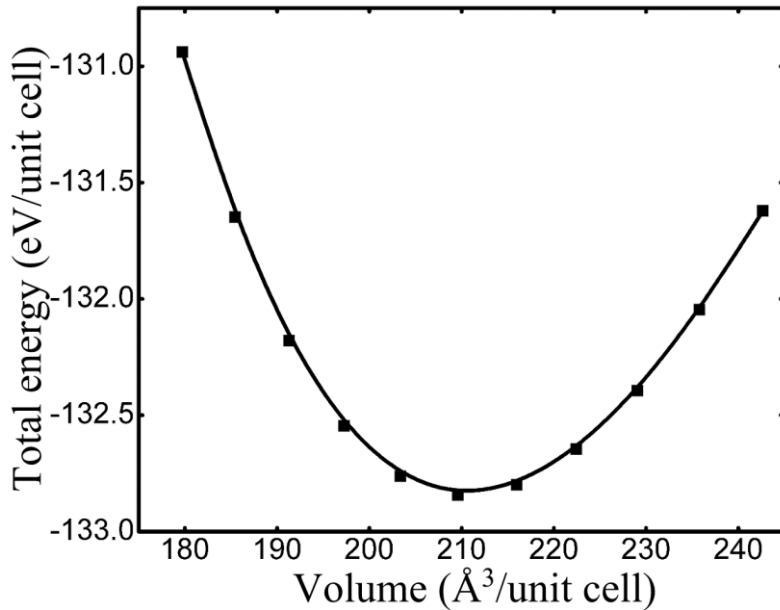


Fig. 3. 2 : Optimized volumes of the LiCAF crystal. The curve is fitted using the Murnaghan equation of state.

This values are larger than our previous LDA results by 0.42 to 5.0 % and are closer to experimental values with a difference ranging only from 0.08 to 0.53 %. In addition, the bulk and Young modulus of the fluoride crystal are also obtained. LiCAF had calculated bulk modulus of 108.01. The calculated Young moduli along the a - and c -axes are 105.32 and 94.89 GPa for LiCAF.

LiCAF's Young moduli are close to the observed isotropic Young modulus approximation of 96 GPa, although particular axis or direction of compression was not mentioned [78]. The Young modulus is defined for a compression along one axis or direction, while the bulk modulus is defined for a compression where the pressure is applied uniformly along all directions.

3. Equilibrium structure of LiCAF crystal

After optimization the structure of LiCAF crystal, the optimized lattice constants, volume and the positions of atoms are using for electronic band structure and optical properties calculations at equilibrium structure (non-pressure).

3.1 Electronic band structure

Figure 3. 3 illustrates the electronic band structure diagrams of LiCAF crystal along the high symmetry lines of the first Brillouin zone. The maximum of the valence band is located at the k -point between M and K. Similar to the conduction band minima situated at the Γ point, this material is to found have indirect band gap of 12.23 eV. Compared with experimental results as also shown in Table 3. 3, our present calculation gives only a difference of 3.30 or 10.51 % which all indicate good agreement within an acceptable uncertainty. We have previously reported different results for the band structures of these fluoride crystals. Aside from the different locations of the valence band maxima, the computed LDA band gap for LiCAF was 8.02 eV. This value corresponds to

a difference of 25.91 % when compared to experimental results. Even though it gives reliable band dispersions, LDA underestimates the band gap severely in contrast to the hybrid PBE functional. We conclude that PBE + exact exchange is a better approximation of the band gap energies than LDA.

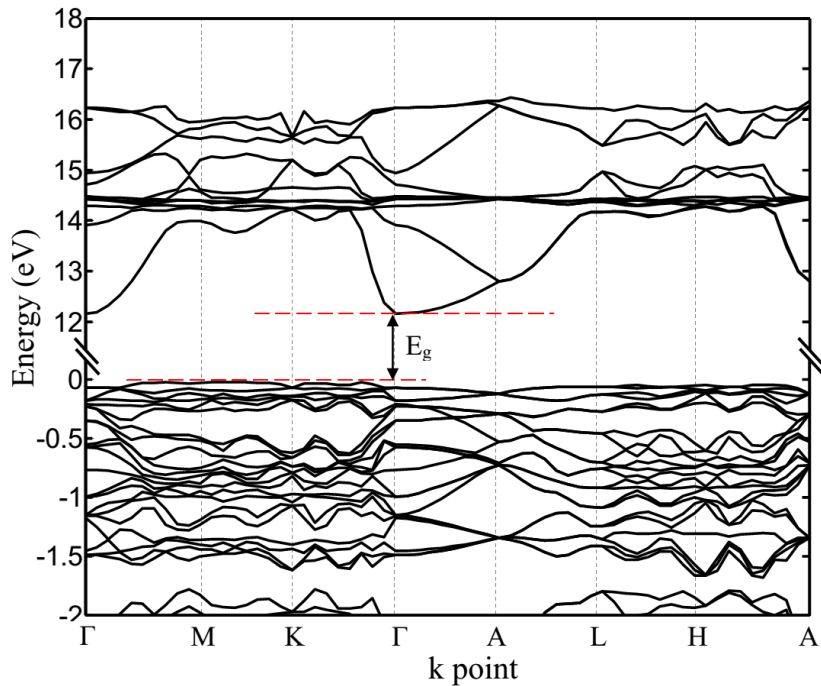


Fig. 3. 3: Simulated electronic band structure diagram of LiCAF crystal having indirect band gaps of 12.23 eV.

Table 3.3 Comparison of lattice constants, crystal volume, bulk modulus, and band gap energy for LiCAF crystal from previous calculations and experimental results. The values inside the parentheses indicate the percent differences from the experimental results.

Parameters	Previous results (LDA) [20]	Present results (PBE)	Experimental results [12, 13, 79]
Lattice constants (Å)			
a	4.97 (0.72)	4.99 (0.30)	5.01
c	9.59 (0.52)	9.66 (0.23)	9.64
Volume (Å³)	205.76 (1.81)	208.45 (0.53)	209.55
Bulk modulus (GPa)	--	108.01	93.4
Band gap E_g	8.02 (36.60, 27.55) (direct)	12.23 (3.30, 10.51) (direct)	12.65 11.07

3.2 Density of state of LiCaAlF₆ crystal

Figure 3. 4 shows the total and partial DOS for LiCAF crystal. For this fluoride compound, the lower and upper parts of the valence band are derived from Al 3s and Al 3p and from F 2p, respectively. Similarly, the conduction band minimum of this crystal is derived from Al 3s. Ca 4s also contribute to the conduction band of the LiCAF crystal.

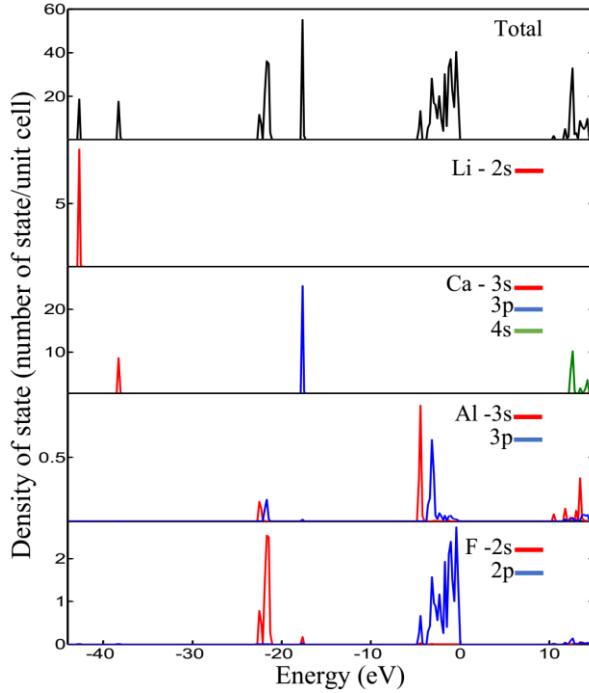
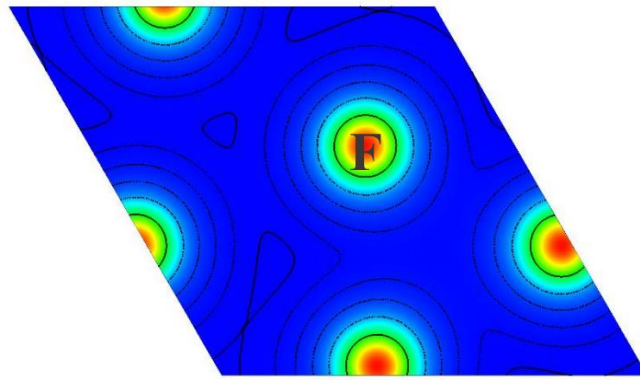


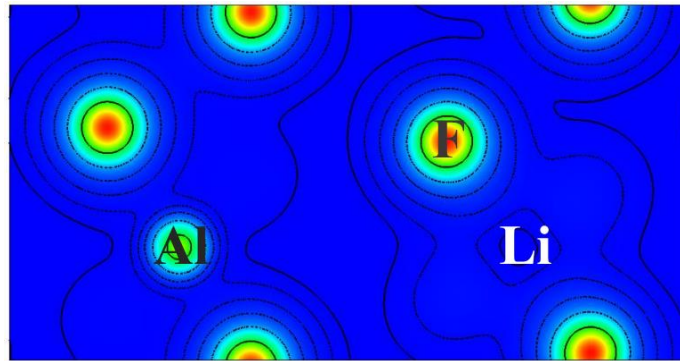
Fig. 3.4 The total and partial density of states of perfect LiCAF crystal

3.3 Charge density distributions of LiCaAlF₆ Crystal

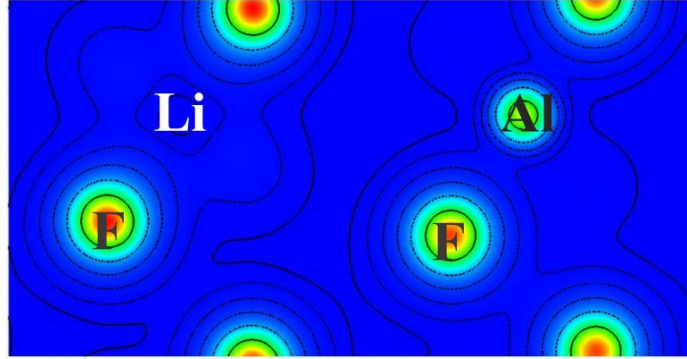
The valence charge density distributions in the LiCAF crystal are calculated to illustrate more clearly the electronic structure and bonding in this fluoride material. We pick up several crystal planes perpendicular to each axis to analyze the bonding of atoms. The charge density distributions of LiCAF crystal in the different planes (a) 001 plane, 1.45 Å from the origin perpendicular to the z-axis, (b) 010 plane, 2.80 Å from the origin perpendicular to the y-axis and (c) 100 plane, 2.85 Å from the origin perpendicular to the x-axis are shown in the Fig. 3.5. In the Fig. 3.5 (a), fluorine is even a much smaller ion but its bonding is quite intensity. The Fig. 3.5 (a) and (b) show that the bonding between fluorine and aluminum is much stronger than bonding between fluorine and lithium.



(001) 1.45 Å from the origin perpendicular to the z-axis



(010) 2.80 Å from the origin perpendicular to the y-axis



(100) 2.85 Å from the origin perpendicular to the x-axis

Fig. 3. 5 The charge density distributions of LiCAF crystal in the different planes (a) 001 plane, 1.45 Å from the origin perpendicular to the z-axis, (b) 010 plane, 2.80 Å from the origin perpendicular to the y-axis and (c) 100 plane, 2.85 Å from the origin perpendicular to the x-axis

This difference can be explained by the distance between atoms. In the LiCAF crystal structure as shown Fig. 3. 1, six fluorine atoms surround a aluminum atom with the distance is around 1.83 Å while that distance for fluorine and lithium is around 2.02 Å. Moreover, the positive charges at the valence of Al and Li are 3 and 1, respectively. The distributions of charge around the anion and cation are spherical, supporting that LiCAF is a ionic crystal.

3.4 Optical properties of LiCaAlF₆ crystal

Our first-principles calculations of the optical properties of the LiCAF crystals are based on the complex dielectric function which represents the linear response of the system to an external electromagnetic field with a small wave vector. In our calculations, the excitonic effect was ignored, while the local field effect was considered. The complex shift in the Kramers-Kronig transformation is only 0.1, which is a perfectly acceptable value. Fig. 3. 6 shows the real and imaginary parts of the he complex dielectric functions of the LiCAF crystal. The Kramers-Kronig relation is used to extract the real part from the imaginary part of the dielectric function. An important quantity from the real part of the dielectric constant is the zero frequency limit. This value where the energy is equal to zero, i.e. $\varepsilon_1(\omega=0)$, represents the static dielectric constant. The static dielectric constants of LiCAF is 1.31. The static dielectric constant consists of ionic and electronic contributions, and these contributions

can be calculated from the dielectric constant and the refractive index. The ionic contributions are found to be very small for LiCAF crystal. On the other hand, the important information from the imaginary part of the dielectric constant are the orbital transitions which can be matched to the DOS (Fig. 3. 4). LiCAF has four peaks located at 10.97, 14.40, 30.17, and 34.28 eV which correspond to the transitions from F 2p to Al 3s, from F 2p to Ca 4s, from Ca 3p to Al 3s, and from Ca 3p to Ca 4s, respectively.

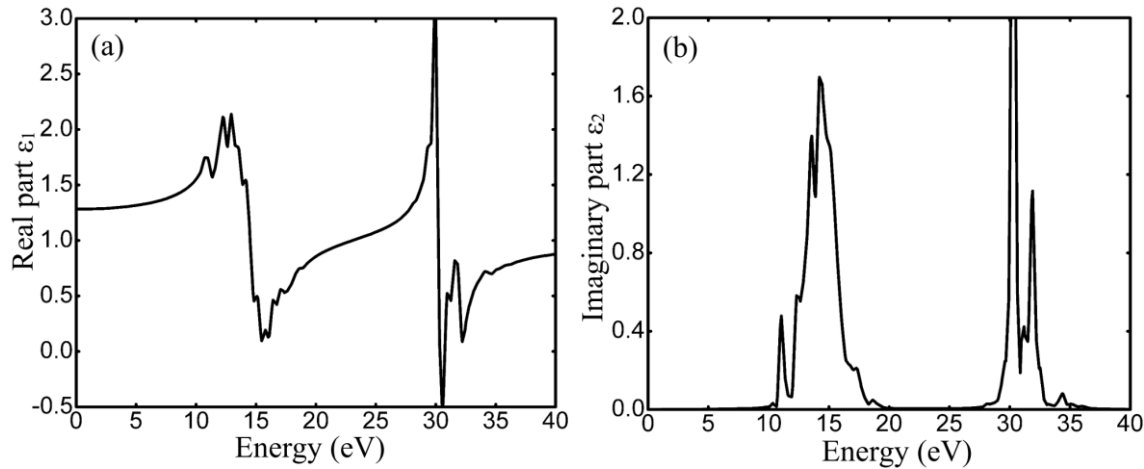


Fig. 3. 6 The real (a) and imaginary (b) parts of dielectric function of LiCAF crystal.

Furthermore, Fig. 3. 7 shows the refractive indices and absorption coefficients of the LiCAF crystal. LiCAF has maximum refractive index and absorption coefficient at 13.03 eV. Since LiCAF is a birefringent crystals, it has similar ordinary and extra-ordinary components of refractive indices [80]. The constant refractive indices for ordinary and extra-ordinary components are 1.30 and 1.31 respectively. Our results were compared with experimental

values, it agrees that extra-ordinary part is greater than ordinary of refractive indices and it differs by around 8%. For a better comparison with experimental results, the transmittance spectra of LiCAF crystal is obtained from the calculated absorption spectra. Our transmittance spectra spanning from the VUV to the visible wavelengths are in good agreement with Ref.[81]. LiCAF has good transmittance down to the VUV region. In addition, previous experimental investigations report the LiCAF absorptions around 125 nm which was initially attributed to possible color centers or impurities [2, 3]. Based on our calculations, this observed absorption can be explained by the F 2p to Al3s transition instead of the presence of unintentional absorption centers.

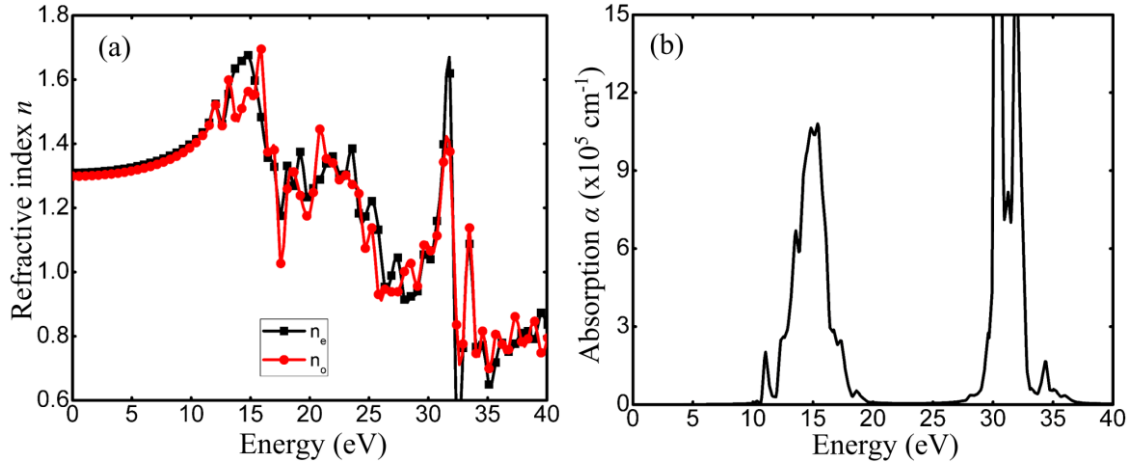


Fig. 3. 7 The (a) refractive index and (b) absorption coefficient of LiCAF crystal.

3.5 Comparison of Ce:LiCAF and Ce:LiSAF crystals on solarization effect

Excited state absorption (ESA), which is prevalent in rare-earth-doped fluorides, has been observed in both Ce:LiCAF and Ce:LiSAF. However, experimental investigations reveal that Ce:LiSAF experiences ESA to a greater extent compared to Ce:LiCAF. Several papers have suggested that ESA is a result of a transition from the $5d$ excited state energy level to the conduction band [16, 83, 84]. Therefore, the onset of the ESA band strongly depends on the host where a $5d$ level that is closer to the conduction band will manifest ESA with greater probability. Our calculations show that LiCAF has a higher band gap compared with LiSAF. Therefore, the $5d$ -to-conduction band distance in Ce:LiCAF is expected to be smaller compared to Ce:LiSAF.

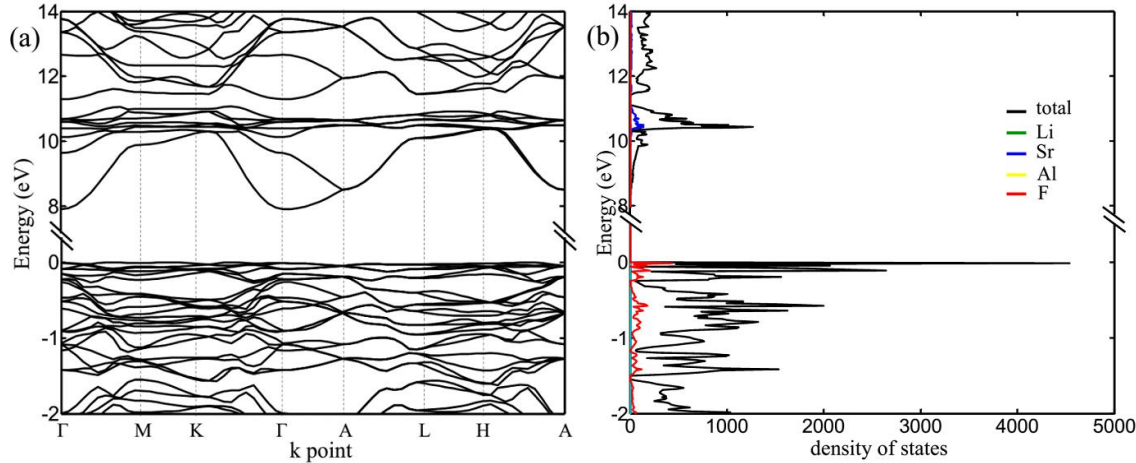


Fig. 3. 8 (a) Electronic band structure and density of states of LiSrAlF_6 crystal

Associated with the strong ESA is solarization [81-87], which occurs when an electron promoted from the $5d$ level gets trapped in an impurity

present in the conduction band as shown in Fig. 3. 9. Solarization is the creation of color centers under UV excitation and is manifested by the observation of broad absorption bands in the energies other than the band gap [85]. When doped with trivalent cerium, the Ce^{3+} ions in the LiCAF or LiSAF structure are presumed to lie in the Ca^{2+} or Sr^{2+} octahedral sites [82]. The size of Ce^{3+} ion (1.15 Å) is about the same as the size of the Ca^{2+} ion (1.14 Å), but smaller than the Sr^{2+} ion (1.27 Å). The CeF_6 cluster, therefore, has to be extended in LiSAF to compensate for this. Indeed, it has been reported that LiSAF is more prone to cracks and inclusions during crystal growth than LiCAF under the same crystal growth conditions [3]. The more pronounced ESA as described above combined with the greater amount of impurities leads to significant solarization in Ce:LiSAF.

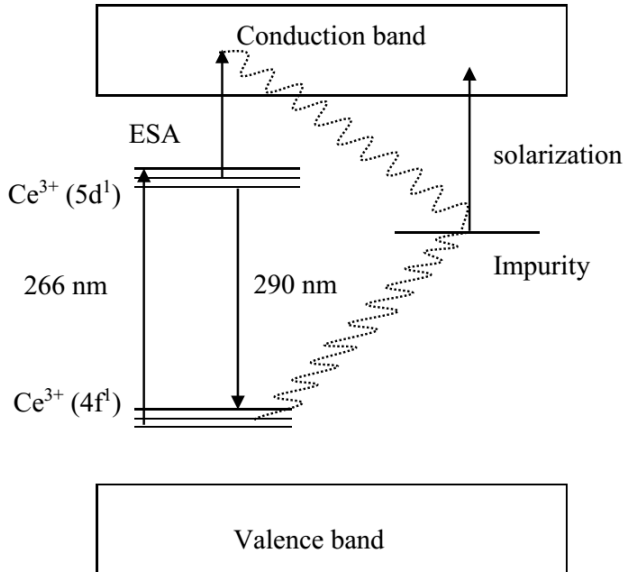


Fig. 3. 9 Schematic diagram of ESA and solarization effect in Ce:LiCAF and Ce:LiSAF crystals

4. Uniform volume compression

The fluorescence emission and absorption edge of wide band gap materials are highly dependent on the band gap energy. Band gap engineering is generally achieved through lattice distortion by changing the material composition with impurity doping. Since this method often leads to altered material properties and growth procedures, material compression under high pressure is a remarkable alternative in changing the lattice parameters while keeping the composition constant. To identify the effects of high pressure on the properties of fluoride materials, the dependence of the crystal volume and electronic band structure on the pressure applied uniformly on the crystals is also investigated.

4.1 Electronic band structure of LiCaAlF₆ crystal

Figure 3. 10 illustrates the simulated LiCAF band structure at different pressures (uniform volume compression) when the ions are allowed to relax after compression. At equilibrium volume, LiCAF has an indirect band gap of 12.23 eV (Fig. 3. 10 a), which is in good agreement with the experimental value of 12.65 eV [12].

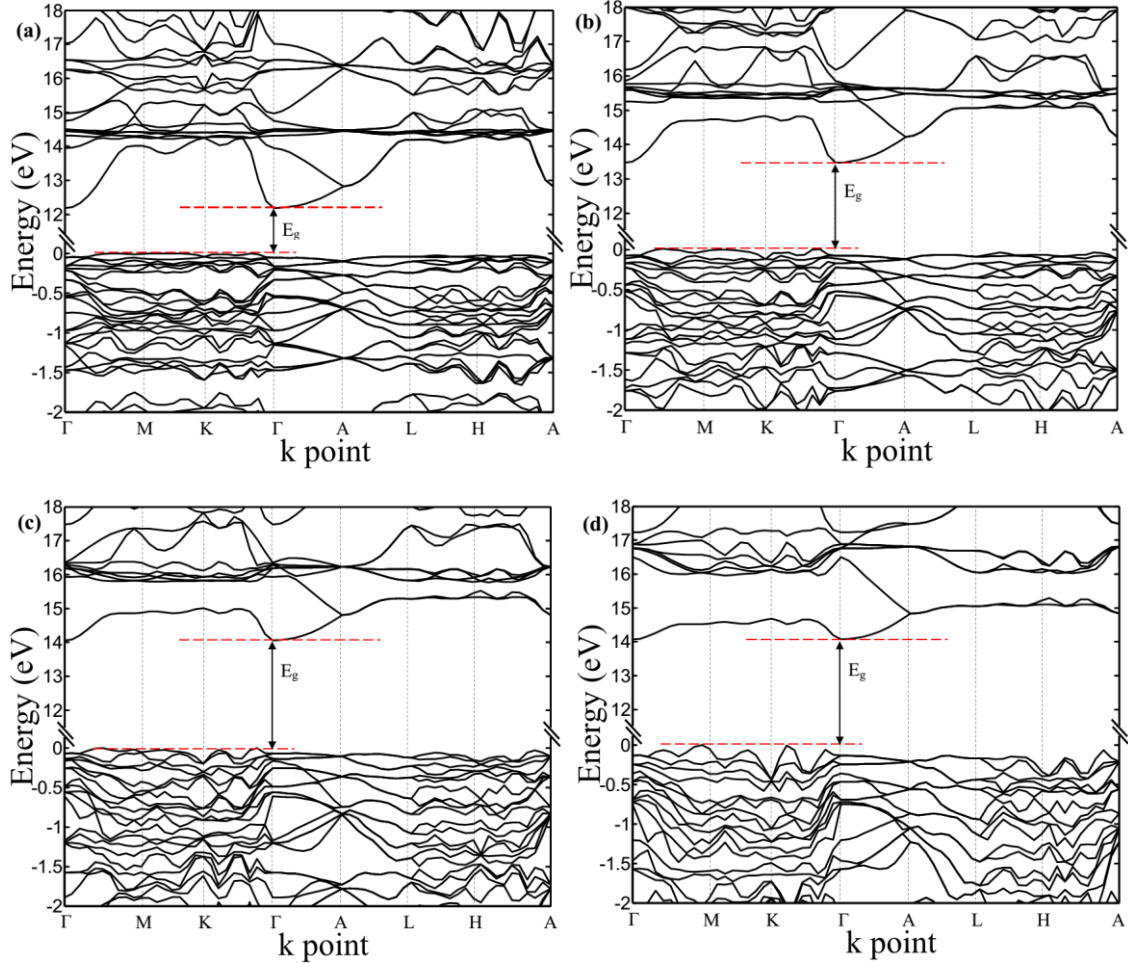


Fig. 3. 10 Simulated electronic band structure diagrams of the LiCAF crystal at (a) 0, (b) 16.32, (c) 48.26 GPa, and (d) 110.10 GPa applied pressure. The band gap is close to becoming direct at 110.10 GPa applied pressure.

The valence band maximum is located at the k -point between M and K, while the conduction band minimum is situated at the Γ -point. At 16.32 GPa (Fig. 3. 10b), the lattice constants are compressed by 5% (volume is compressed by 14.26%), and the indirect band gap increases to 13.32 eV. Increasing the pressure to 48.26 GPa (Fig. 3. 10c) results in the compression of the lattice constants and volume by 10% and 27.10%, respectively. As a result, the indirect band gap increases to 14.13 eV. When the applied pressure reaches

110.10 GPa, the lattice constants reduce to 85% of their equilibrium values, and the crystal volume is compressed to 61.41% (128 \AA^3). The band gap is close to becoming direct.

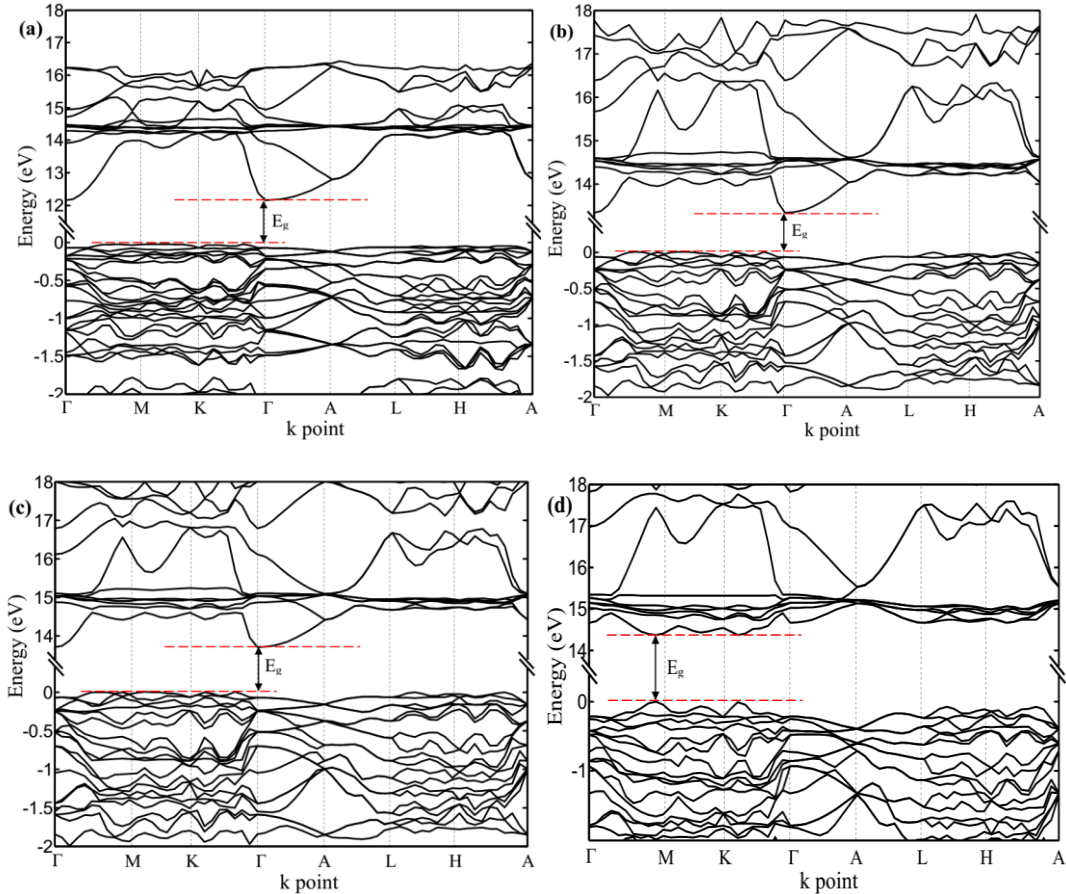


Fig. 3. 11 Simulated electronic band structure diagrams of the LiCAF crystal at (a) 0, (b) 16.32, (c) 48.26 GPa, and (d) 110.10 GPa applied pressure. The band gap shift to direct at 110.10 GPa pressure, assuming picosecond experimental time scales.

Figure 3. 11 shows the LiCAF band structures when pressure is applied in the picosecond scale such that ions are not allowed to relax. The results are similar to the relaxed-ion state at low pressure. Intriguingly, the band gap shifts from indirect to direct, with a value of 14.21 eV, at 110.10 GPa. In this

instance, both the valence band maximum and the conduction band minimum are located near the M-point. This interesting result clearly demonstrates that pressure can induce an indirect-to-direct band gap transition in LiCAF.

4.2 Density of state of LiCaAlF₆ crystal

Figure 3. 12 shows the total and partial density of states of the LiCAF crystal at 0 (Fig. 3. 12a) and 110.10 GPa for relaxed (Fig.3. 12b) and unrelaxed ions (Fig. 3. 12c). At 0 GPa, the valence band is mainly derived from F 2p, (add comma) with minor contributions from Al 3s and Al 3p. In addition, the conduction band is mainly derived from Ca 4s, and the conduction band minimum is partly derived from Al 3s. The first absorption peak or transmission edge that is observed in experimental investigations of LiCAF arises from this minor Al 3s contribution [2, 13]. At 110.10 GPa, the valence band maximum is still derived from F 2p and the conduction band minimum is still derived by Al 3s when the ions are allowed to relax. However, if the ions are not allowed to relax, the conduction band minimum is now derived from Ca 4s since the Al 3s bands are shifted to higher energy.

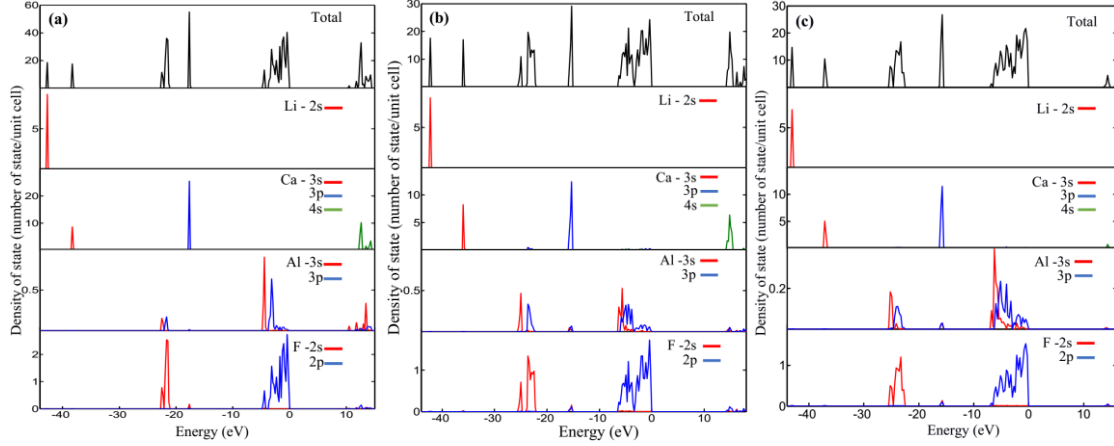


Fig. 3. 12: Total and partial density of states of the LiCAF crystal at (a) 0 and 110.10 GPa applied through uniform volume compression for the case when (b) ions are not allowed to relax and (c) ions relax.

4.3 Pressure dependence of band gap energy and volume

Figure 3. 13 shows the unit cell volume and band gap of the LiCAF crystal at different pressures (uniform volume compression). The volume is inversely proportional to pressure, while the band gap monotonically increases with increasing pressure within the range of 0 to 50 GPa. At 0 GPa (equilibrium), the LiCAF crystal has a unit cell volume of 208.45 \AA^3 and an indirect band gap energy of 12.23 eV. Applying a pressure of ~ 50 GPa compresses both the a and c lattice constants by 10 %. The volume also compresses uniformly by ~ 27 %, and the band gap increases by ~ 16 %. The computed crystal volumes are in excellent agreement with experiment, differing only by 0.13-0.50% in the pressure range 0-15 GPa [75].

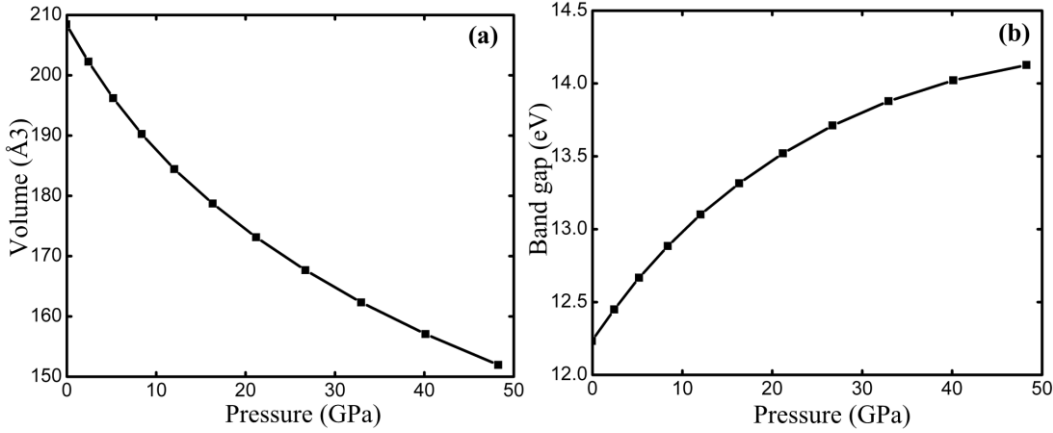


FIG. 3. 13: (a) Unit crystal volume and (b) band gap energy of the LiCAF crystal at different pressures applied through uniform volume compression.

The band gap increases monotonically with pressure up to 50 GPa.

This high-pressure increase in the band gap and the transition from indirect to direct band gap can be explained by the Madelung potential. The binding energy of ionic crystals results from the electrostatic interaction of oppositely charged ions which is strongly dependent on the distance of charges. When pressure is applied on the crystal, the volume is compressed, and the attractive potential of electrons and atoms increases due to dense packing. The valence band which is mainly derived from the p-orbital is more localized compared to the conduction band which is mainly derived from the s-orbital. The conduction bands are greatly shifted to energies higher than the shifts of the valence bands resulting in an increase of the band gap energy. Furthermore, the conduction band minimum at the Γ -point is occupied by Al 3s, while the lower part of the conduction band near the M-point is occupied by Ca 4s. At a high pressure of 110.10 GPa, the electronic bands of Al 3s shift to higher energies than those of Ca 4s causing the band gap transition from

indirect to direct. Based on this phenomena, the electronic behavior of LiCAF can be then modified by applying pressure on the crystal.

As a phase transition from the LiCAF-I to the higher pressure LiCAF-II structure has been experimentally observed between ~ 7 and 9 GPa, we tested our simulation parameters by running optimizations for both structures at pressures ranging from 0 to 50 GPa. For these simulations, we used the hydrostatic pressure model in order to best mimic the experimental conditions, allowing the ions to relax at each set pressure. Within our model, LiCAF-II optimizes to the LiCAF-I structure for pressures between 0 and 4 GPa. For pressures 4 – 7 GPa, we predict the LiCAF-I structure to be more stable. The crystal structures are nearly degenerate between 7 and 10 GPa, with the phase transition occurring at 9.7 GPa, in excellent agreement with the experimental results. The band gaps and crystal volumes predicted for the two structures are nearly identical in the pressure range 0 – 50 GPa, differing by a maximum of 0.15 eV and 1 \AA^3 , respectively.

5. Pressure dependence of band gap energy under uniaxial compression

Figure 3. 14 shows the total energy as a function of the a and c lattice constants. The total energies are expressed in terms of the Murnaghan equation of state. The bulk modulus and the compressibility (which is inversely proportional to the bulk modulus) are also obtained. Along the a -axis, LiCAF has an equilibrium lattice constant of 4.99 \AA , a bulk modulus of 105.32 GPa,

and a compressibility of 9.49 MPa^{-1} . On the other hand, along the c-axis, LiCAF has an equilibrium lattice constant of 9.66 \AA , a bulk modulus of 94.89 GPa , and a compressibility of 10.54 MPa^{-1} . A lower bulk modulus and higher compressibility indicate that the c-axis is easier to compress than the a-axis.

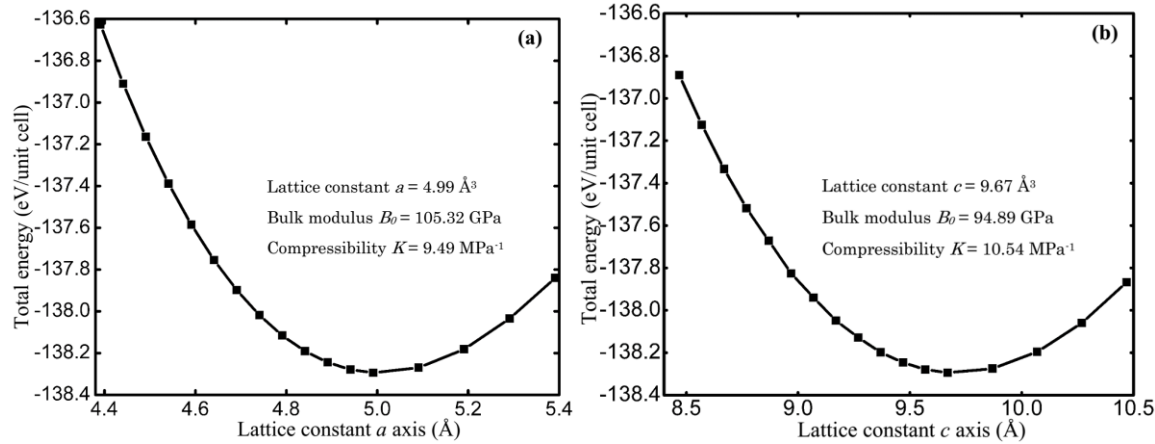


FIG. 3.14 : Optimized (a) *a* and (b) *c* lattice constants of the LiCAF crystal.

Figure 3.15 shows the lattice compression ratio and band gap energy of the LiCAF crystal at different pressures applied through uniaxial compression. Pressures in the range of 0-13 GPa are applied to the *a*-axis and *c*-axis, separately. Both lattice constants steadily decrease with increasing pressure. At $\sim 13 \text{ GPa}$, the lattice constants compress by 12.02% and 12.42% along the *a*- and *c*-axis, respectively. On the other hand, the band gap increases with increasing pressure up to $\sim 7.6 \text{ GPa}$, then decreases for higher pressures. Maximum band gap energies of 12.52 and 12.63 eV are achieved when 7.6 GPa is applied to the *a*-axis and *c*-axis, respectively. These results suggest that it is

more effective to apply pressure along the c-axis in order to increase the band gap.

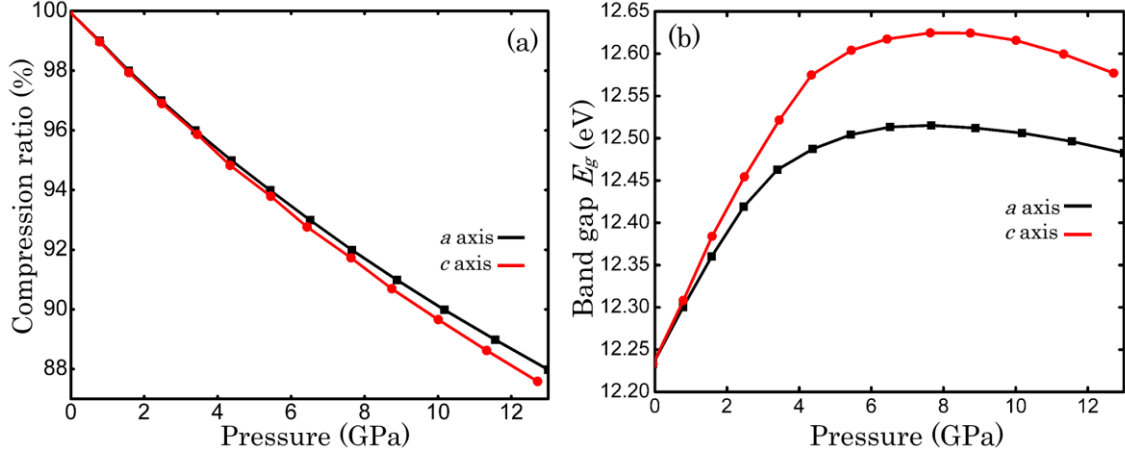


FIG. 3. 15: (a) Lattice constant compression and (b) band gap energy of the LiCAF crystal at different pressures applied through uniaxial compression.

Maximum band gap energies of 12.52 and 12.63 eV are achieved with uniaxial compression along the *a*-axis and *c*-axis, respectively using 7.6 GPa applied pressure.

6. Conclusions

The electronic and optical properties of perfect LiCAF crystal were calculated based on DFT using PBE functionals employing 35 % exact exchange. The LiCAF was found to have indirect band gap of 12.23 eV. This result differs only by around 3% from the experimental value. Our calculated electronic band structure is helpful to explain the small polarization effect on Ce:LiCAF comparing with Ce:LiSAF crystal. Using hybrid functional, the optical properties of LiCAF crystal were firstly calculated and it is giving the

explanation of the experimental absorption at around 130 nm. The dependence of the band gap energy on pressure applied by uniform volume and uniaxial compression were also investigated. Through uniform volume compression, LiCAF's indirect equilibrium band gap of 12.23 eV would shift to a direct band gap of 14.21 eV at 110.10 GPa and picosecond time scales, arising from the energetic swap of the Al 3s and Ca 4s orbitals. Through uniaxial laser-shock compression, we estimate that the LiCAF crystal has a band gap of \sim 12.60 eV. Our findings have highlighted the change in the electronic behavior of this fluoride compound upon application of high pressure. These results can be used to instruct the development of tunable, compact, solid-state VUV light sources based on LiCAF as a laser host material.

Supplemental Information

Table S3. 1. Lattice constants, crystal volumes, and band gap energies of the LiCAF at different pressures applied through uniform volume compression. The values inside the parentheses indicate the percent differences compared to the equilibrium value (0 GPa).

Pressure (GPa)	Lattice constants (Å)		Crystal volume (Å ³)	Band gap (eV)
	a	c		
0	4.99	9.66	208.45	12.23
16.32	4.74 (5.00)	9.18 (5.00)	178.72 (14.26)	13.32 (8.91)
48.26	4.49 (10.00)	8.69 (10.00)	151.96 (27.10)	14.13 (15.54)
61.10	4.24 (15.00)	8.21 (15.00)	128.01 (38.59)	14.21 (16.19)

Table S3. 2. Lattice constants, crystal volumes, and band gap energies of the LiCAF at different pressures applied through uniaxial compression along the a-axis. The values inside the parentheses indicate the percent differences compared to the equilibrium value (0 GPa).

Pressure (GPa)	Lattice constants (Å)		Crystal volume (Å ³)	Band gap (eV)
	a	c		
0	4.99	9.66	208.45	12.23
3.40	4.79 (4.01)	9.66	200.10 (4.01)	12.46 (1.88)
7.66	4.59 (8.02)	9.66	191.74 (8.02)	12.52 (2.37)
13.01	4.39 (12.02)	9.66	183.39 (12.02)	12.48 (2.04)

Table S3. 3. Lattice constants, crystal volumes, and band gap energies of the LiCAF at different pressures applied through uniaxial compression along the c-axis. The values inside the parentheses indicate the percent differences compared to the equilibrium value (0 GPa).

Pressure (GPa)	Lattice constants (Å)		Crystal volume (Å ³)	Band gap (eV)
	a	c		
0	4.99	9.66	208.45	12.23
3.45	4.99	9.26 (4.14)	199.82 (4.14)	12.52 (2.37)
7.63	4.99	8.86 (8.28)	191.19 (8.28)	12.63 (3.27)
12.72	4.99	8.46 (12.42)	182.71 (12.35)	12.58 (2.86)

Chapter 4

Experimental results for uniaxial compression of LiCaAlF_6 crystal

Wide band gap materials are desirable for the development of short wavelength optical devices. Fluoride compounds have been shown to have wide band gaps that allow them to be highly transmitting down to the VUV region. In addition, fluoride compounds with direct band gap transitions are needed in order to develop short wavelength solid-state light emitting devices with appreciable emission intensities. This is generally achieved through band gap manipulation where the lattice is distorted, by controlling the composition of the material or by doping the material with impurities. These methods often lead to completely different material properties and growth procedures. Another way of achieving direct band gap transition is by material compression under high pressure. This technique is remarkable at changing the lattice parameters while keeping the composition constant. A silicon-germanium (Si-Ge) semiconductor superlattice was predicted to have an indirect to direct band

gap transition by a substrate in 1987 [30]. Moreover, band gap manipulation has also been reported for lithium fluoride (LiF) under high pressure [31]. Application of 70 GPa hydrostatic pressure to LiF transformed it from a direct to an indirect band gap insulator, simultaneously altering the optical properties of the crystal.

1. Experimental set up

Room-temperature X-ray diffraction (XRD) spectroscopy of a nominally undoped LiCAF crystal were performed, using the NW14A beam line of the Photon Factory Advanced Ring of the High Energy Accelerator Research Organization (KEK). Laser-shock compression is a new experimental technique which is used to abruptly apply pressure to a material. Uniaxial compression is achieved by focusing a 10 J, 500 ns laser pulse onto the material as shown in Fig. 4. 1. This provides an estimated laser-shock pressure of \sim 11 GPa [88-90]. In our experiment, the laser beam was oriented incident to either the a- or c-axis of the crystal. The XRD patterns were then obtained from single-shot diffraction images. The uncompressed and compressed LiCAF signatures were both present in the patterns. The compressed signature was identified by drawing tangent lines. Each diffraction point was then converted to a line pattern, where each end point on the pattern corresponds to a diffraction point before compression. The experimental results were compared with Laue XRD simulations to determine the a and c lattice compression after laser shock. The maximum compression ratio at each time delay was estimated

assuming that the lattice constant changes only along the direction of compression.

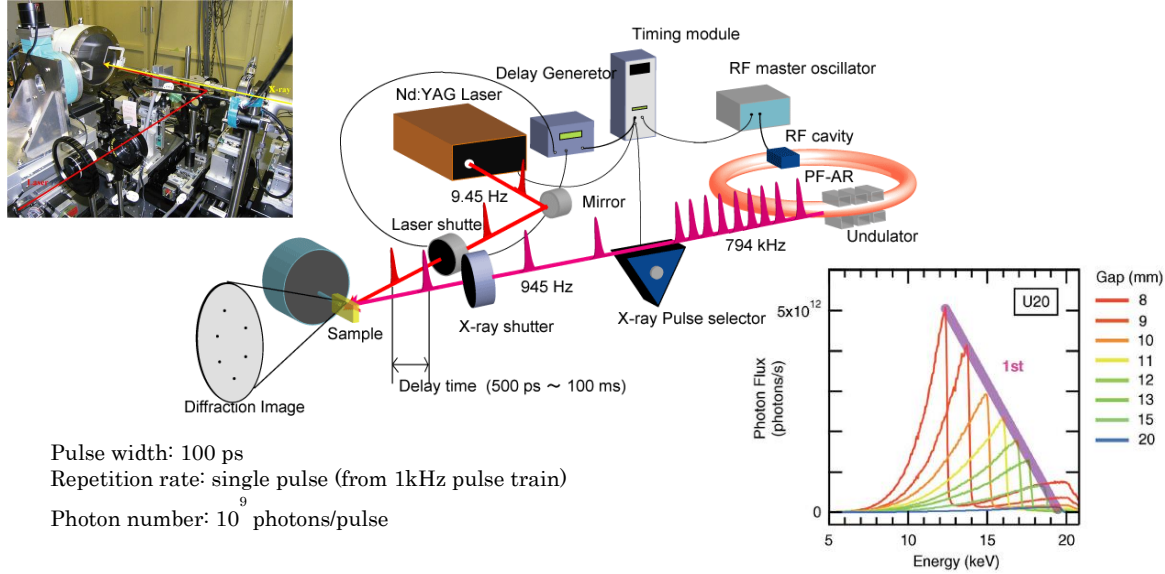


Fig. 4. 1 The experimental set up for uniaxial compression of LiCAF crystal by laser-shock

2. X-ray diffraction results

Figures 4. 2 and 4. 3 show the tangent XRD patterns of the LiCAF crystal obtained using laser-shock compression along the a-axis and c-axis, respectively. The changes along the (4, -1, 2) plane of the crystal are observed within a time delay of 0 to 35 ns. These XRD patterns are then compared to the Laue XRD simulation patterns shown in Figs. 4. 2(h) and 4. 3(h) in order to determine the maximum compression ratio along each axis.

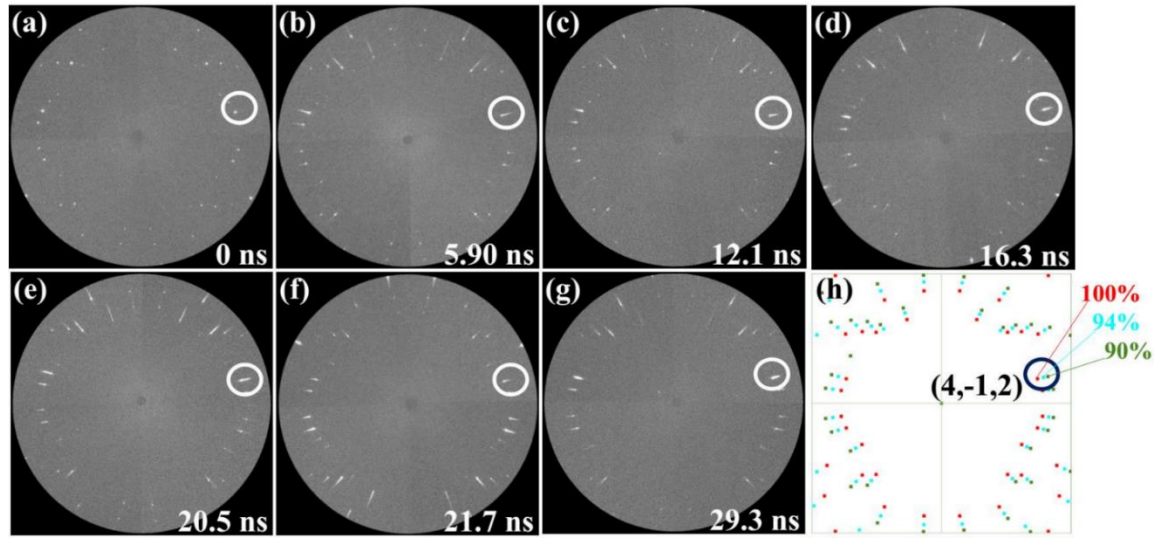


Fig. 4. 2 XRD patterns of the LiCAF crystal with laser-shock compression along the a-axis at different delay times of (a) 0, (b) 5.90, (c) 12.1, (d) 16.3, (e) 20.5, (f) 21.7, and (g) 29.3 ns. h) Laue XRD simulation used to obtain compression ratios.

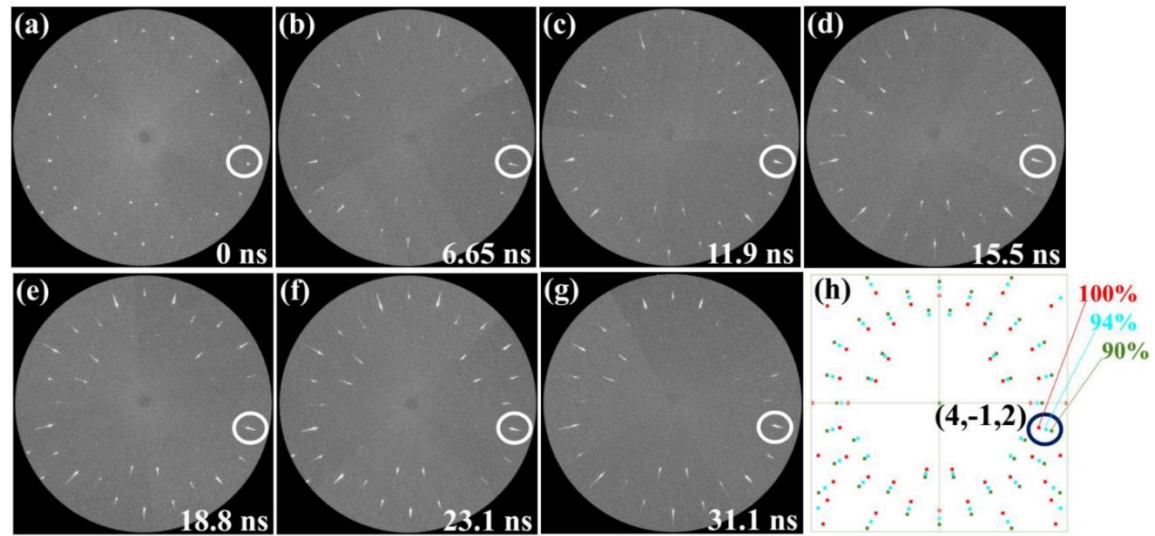


Fig. 4. 3 : XRD patterns of the LiCAF crystal after laser-shock compression along the c-axis at different delay times of (a) 0, (b) 6.65, (c) 11.9, (d) 15.5, (e) 18.8, (f) 23.1, and (g) 31.1 ns. (h) Laue XRD simulation used to obtain the compression ratios.

Figure 4. 4 illustrates the lattice constant compression ratio of the LiCAF crystal with laser shock at different delay times. Comparison with the calculated lattice compression ratios in Fig. 3. 14a indicates that the pressure experienced by the crystal is at most 7.5 GPa. The estimated maximum laser-shock compression ratios are 93.4 (a-axis) and 91.8% (c-axis). The maximum lattice compressions of 6.6% and 8.2% occur at 29.3 and 31.1 ns delays, respectively. The experimental results verify that it is more efficient to compress the LiCAF crystal along the c-axis rather than along the a-axis. By comparing our experimental compression ratios with our numerical results, we predict that LiCAF will have a band gap energy of \sim 12.60 eV, 35 ns after uniaxial laser-shock compression along the c-axis.

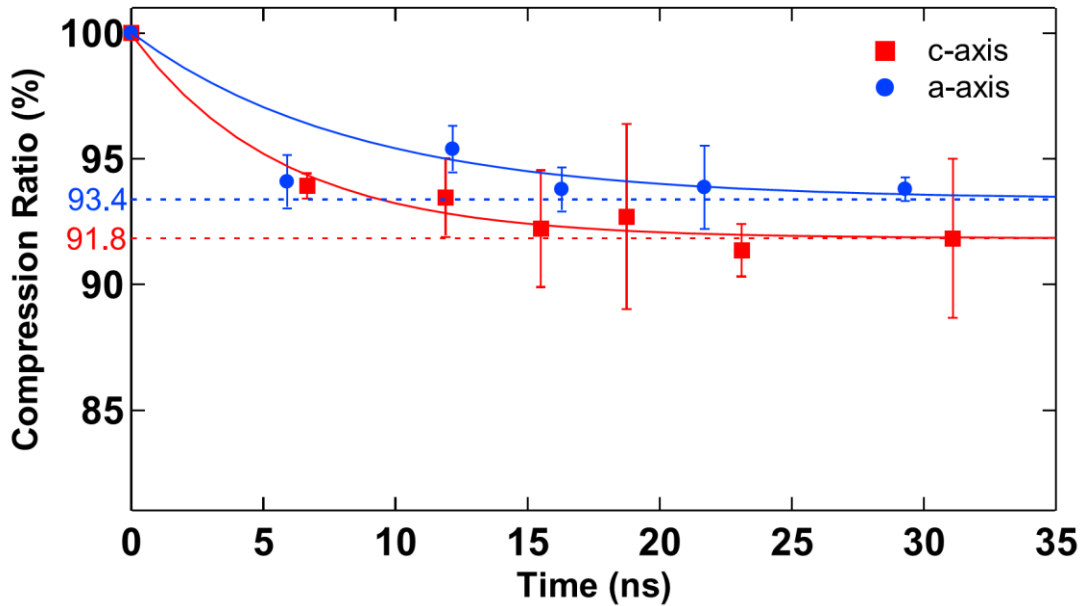


Fig. 4. 4 Lattice constant compression of the LiCAF crystal obtained at different delay times after the laser shock.

4.3 Conclusions

Using 100 – ps X-ray pulses of synchrotron radiation with the laser-shock compression technique, the ratio compression of the a and c-axis of LiCAF crystal were investigated under the pressure of \sim 11GPa. Both a and c-axis of LiCAF crystal show the maximum compression after around 30ns by laser-shock. Comparing with the calculations in the chapter 3, the experimental result also confirmed that the c-axis of LiCAF crystal is easier to compression than the a-axis. Through uniaxial laser-shock compression of the c-axis, we estimate that the LiCAF band gap will increase by \sim 0.4 eV, yielding an experimental ban gap of \sim 13.0 eV. Further experiments with high-power laser system and shorter time scale are doable to confirm our calculation in chapter 3 and to study more about electronic behavior of wide band gap fluoride compounds. We also suggest the high pressure uniform compression by diamond anvil which hopefully can achieve VUV laser emission from direct band gap fluorides.

Chapter 5

The electronic band structure and optical properties of LiYF_4 crystal

Lithium yttrium fluoride (LiYF_4) is one of the scheelite-structured ionic crystals that has been investigated theoretically and experimentally [6, 7, 91, 92]. It has a wide and direct band gap of 10.55 eV [8] and high transparency in the VUV region [4]. LiYF_4 crystal is one of the few fluoride compounds which is direct band gap originally. Based on this property, this crystal can be used not only for laser host material but also for light-emitting diode and optical devices in vacuum ultraviolet and ultraviolet regions. In this chapter, we calculate the electronic band structure and density of states as well as the optical properties of a perfect LiYF_4 crystal as a VUV laser host material. The dependence of these physical quantities on pressure are investigated through uniform volume and uniaxial compression. The LiYF_4 band gap energy and absorption edge can be modified by compressing the crystal uniformly under high pressure.

1. Crystal structure of LiYF_4 crystal

The perfect crystal of LiYF_4 shown in Fig. 5. 1 (a) is used with a unit cell composed of 24 atoms. LiYF_4 is a scheelite-type fluoride with a tetragonal crystal structure belonging to the $I\ 4_1/a$ space group (group number 88) and with four formula units per unit cell. Lithium (Li) and yttrium (Y) ions have 4 and 8 fluorine (F) ions as their nearest neighbors, respectively. The Y and F ions have two nearest neighbor distances of 2.244 and 2.297 Å, while the Li and F ions have a nearest neighbor distance of 1.897 Å [93, 94].

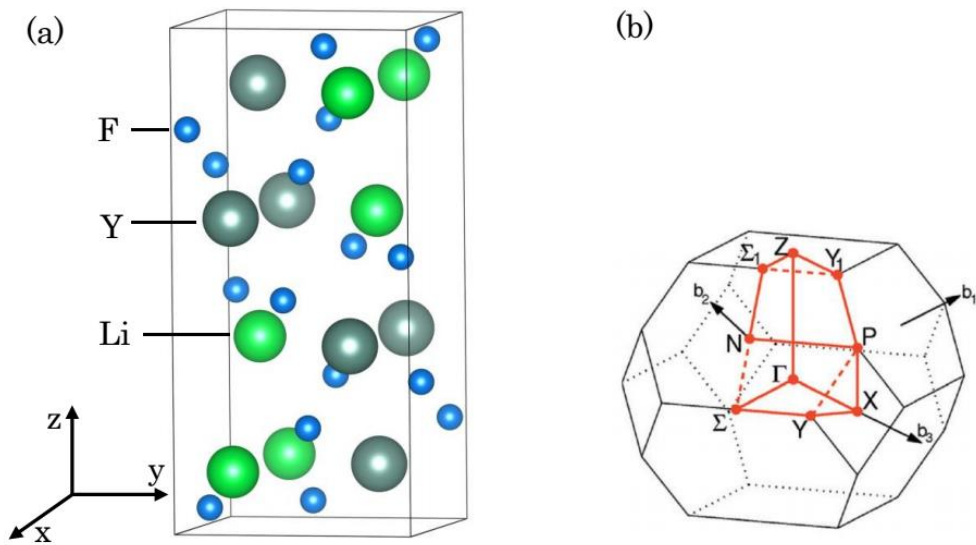


Fig. 5. 1: (a) Scheelite-type structure and (b) first Brillouin zone of tetragonal unit cell of the LiYF_4 crystal.

The reference atomic positions of LiYF_4 crystal are given in the figure 5. 1. The coordinates of high symmetry k points in the first Brillouin zone are shown in the table 5. 2. The k point path to calculate the electronic band structure is following $\Gamma \rightarrow X \rightarrow Y \rightarrow \Sigma \rightarrow Z \rightarrow \Sigma_1 \rightarrow N \rightarrow P \rightarrow Y_1$ [77].

Table 5. 1: the atomic positions of LiYF₄ crystal

	x	y	z
Li	0	1/4	1/8
Y	0	1/4	5/8
F	0.2192	0.5846	0.5436

Table 5. 2: the symmetry points of the first Brillouin zone for tetragonal structure.

Γ	0	0	0
X	0	0	1/2
Y	$-\zeta$	ζ	1/2
Σ	$-\eta$	η	η
Z	1/2	1/2	-1/2
Σ_1	η	$1-\eta$	$-\eta$
N	0	1/2	0
P	1/4	1/4	1/4
Σ_1	1/2	1/2	$-\zeta$

Where $\eta = (1+a^2/c^2)/4$ and $\zeta = a^2/(2c^2)$

3. Optimized volume of LiYF₄ crystal

The total energy per unit cell of the LiYF₄ crystal is plotted as a function of unit cell volume in Fig. 5. 2. At equilibrium, LiYF₄ has an optimized volume of 289.31 Å³ with corresponding lattice constants of 5.17 Å (a –axis) and 10.82 Å (c –axis). These values are very close to the experimental crystal volume and lattice constants with a difference of only less than 1.0 % [93, 94]. The bulk modulus of LiYF₄ is also obtained after fitting with the Murnaghan equation of state [65]. LiYF₄ has a bulk modulus of 75.04 GPa which is lower than the

experimentally measured value of 81 Gpa [95] and the previous calculated value of 94.8 Gpa [96]. Table 5. 3 compares the calculated crystal volume, lattice constants, and bulk modulus of LiYF_4 with previously reported values.

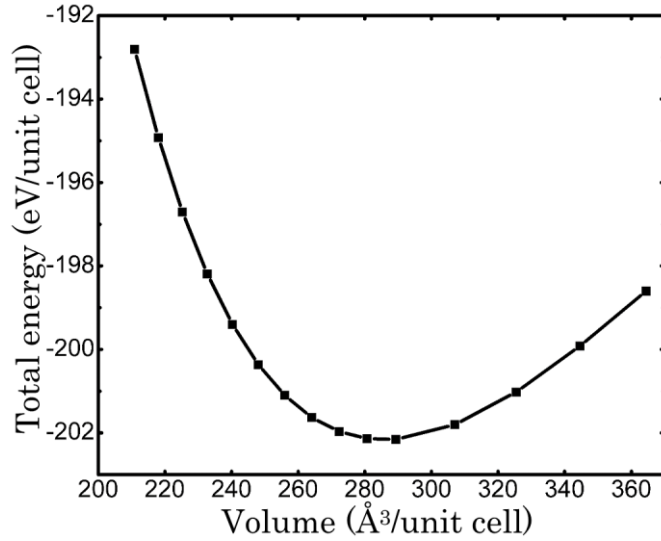


Fig. 5. 2 Optimized volumes of the LiYF_4 crystal. The curve is fitted using the Murnaghan equation of state.

3. Equilibrium structure of LiYF_4 crystal

Based on the experimental reference data such as lattice constants, and the atomic positions of LiYF_4 crystal, we optimized by PBE0 functional with the plane-wave basis cutoff is 500 eV and convergence energy is 10^{-6} , and then the optimized values are using for electronic band structure and optical properties calculations.

3.1 Electronic band structure

The electronic band structure of the LiYF_4 crystal at equilibrium along the high symmetry lines of the first Brillouin zone is shown in Fig. 5. 3. Both the valence band maximum and the conduction band minimum of LiYF are situated at the Γ point. LiYF_4 has a direct band gap energy of 11.09 eV which is higher than the previous reported values of 7.54 or 10.55 eV [8, 11]. Previous reports have used the orthogonalized linear combination of atomic orbitals (OLCAO) [11] or local density approximation (LDA) [8] which often underestimate the band gap energies. By using hybrid functionals that incorporate a fraction of nonlocal Hartree-Fock exact exchange, our calculations overcome the underestimation, resulting to more accurate values.

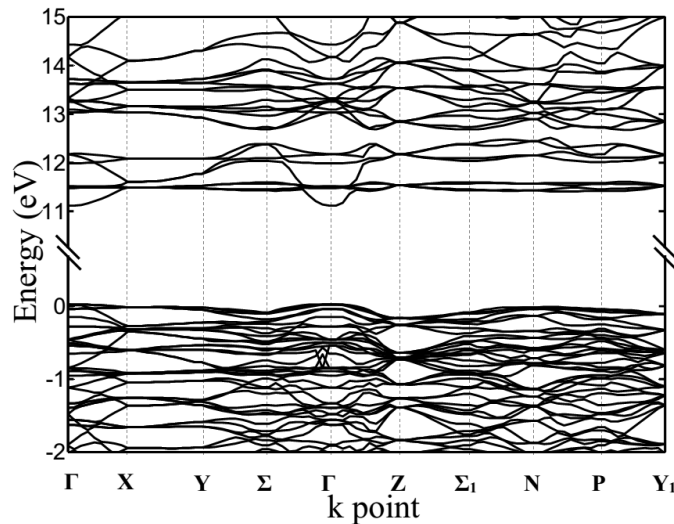


Fig. 5. 3: Simulated electronic band structure diagram of the LiYF_4 crystal having direct band gap of 11.09 eV at gamma point.

Table 5. 3 Comparison of lattice constants, crystal volume, bulk modulus, and band gap energy for LiYF₄ crystal from previous calculations and experimental results. The values inside the parentheses indicate the percent differences from the experimental results.

Parameters	Calculations [11, 70]	PBE0	Experimental [69, 95]
Lattice constants (Å)			
a	5.13	5.17 (0.19)	5.16
c	10.67	10.82 (0.75)	10.74
Volume (Å³)	280.49	289.31 (0.98)	286.51
Bulk modulus (GPa)	94.8	75.04 (7.36)	81
Band gap E_g	7.54 (direct)	11.09 (direct)	--

3.2 Density of state

The total and partial DOS of the LiYF₄ crystal at equilibrium are shown in **Fig. 5. 4**. Three bands can be observed from the total DOS in the range of –25 to 16 eV. The bands from –22.62 to –17.64 eV are due to the F 2s and Y 4p orbitals. On the other hand, the valence band from –3.46 to 0 eV is mainly derived from the F 2p orbital, while the conduction band from 10.70 to 16 eV is mainly derived from the Y 4d orbital. The Li 2s orbital has minor contributions to both valence and conduction bands. The direct band gap of LiYF₄ originates from the transition from F 2p of the valence band maximum to Y 4d of the conduction band minimum.

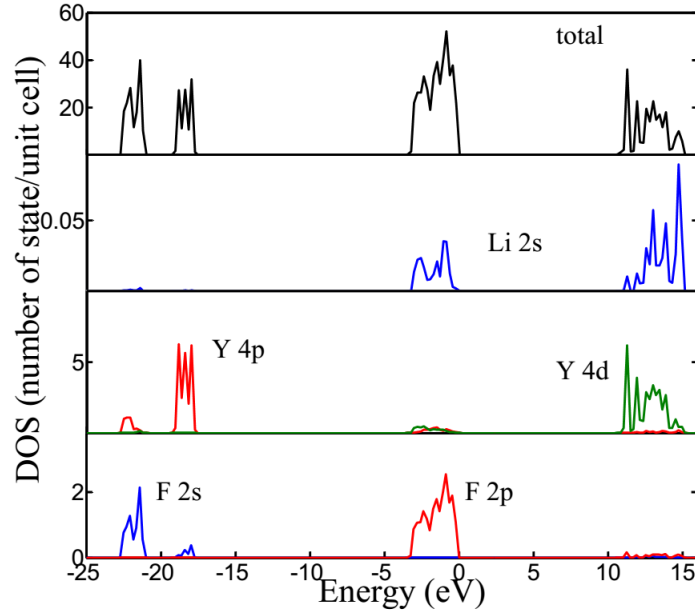
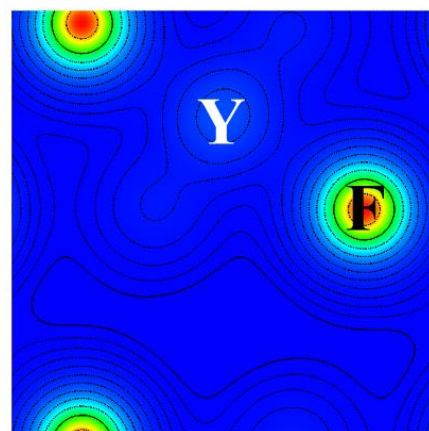


Fig. 5. 4: Total and partial DOS of the LiYF₄ crystal. The red, blue, and green lines represent different orbitals in each atom.

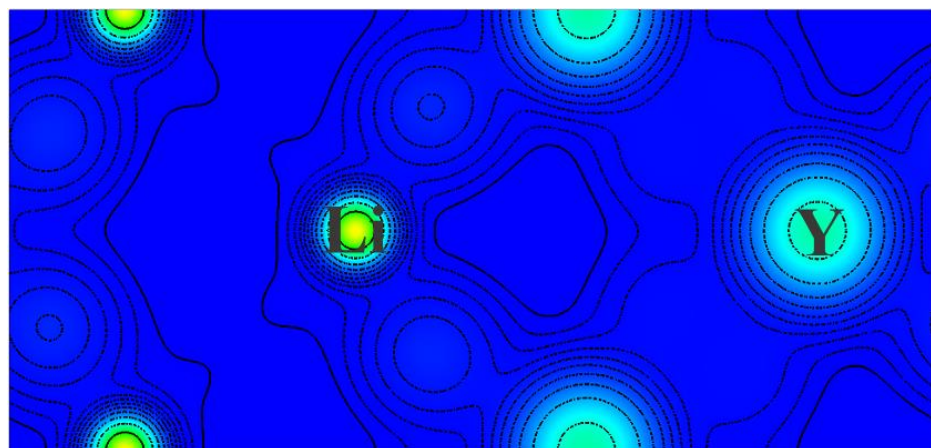
3.3 Charge density

To illustrate more clearly the electronic structure and bonding in LiYF₄, we report on the valence charge distribution of LiYF₄ crystal. Based on this physical property, it may be helpful for doping on this material. Figure 5. 5 shows the charge density at the different planes. Fig. 5. 5 a) is the charge density at the 001 plane, 2.20 Å from the origin perpendicular to the z-axis. Fig. 5. 5 b) is the charge density at the 010 plane, 1.30 Å from the origin perpendicular to the y-axis. Fig. 5. 5 c) is the charge density at the 100 plane, 0.00 Å from the origin perpendicular to the x-axis. From the figure 5. 5, we can see that the bonding between Y and F is much stronger than bonding between Li and F. Li is a much smaller ion compared to F and Y. Charge distribution of Y is less

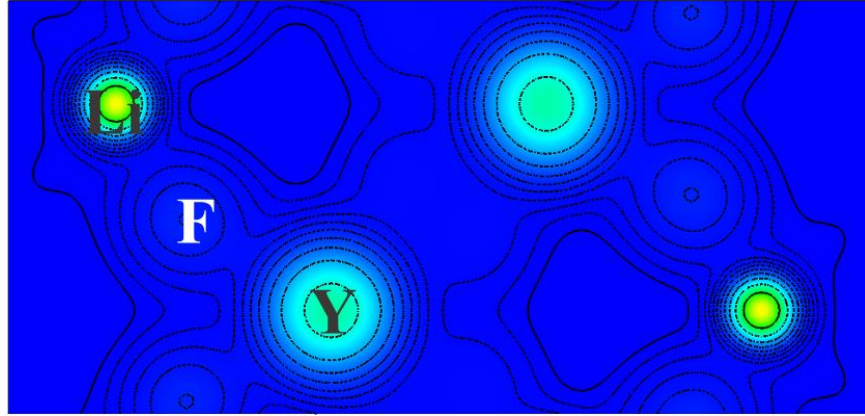
intense than Li and F. Distribution of charges around ions are very spherical, indirectly supporting the viewpoint that LiYF_4 is an ionic crystal. Fig. 5. 5 c) shows the bonding between Li and Y versus to F. The spherical charge density Li ion is much smaller than Y ion, however, the bonding between Li and F ions is stronger than the bonding between Y and F. This is a reason for the Y ion can be easily replaced by other similarity radius cation in the LiYF_4 crystal.



(001) 2.20 Å from the origin perpendicular to the z-axis



(010) 1.30 Å from the origin perpendicular to the y-axis



(100) 0.00 Å from the origin perpendicular to the a-axis

Figure 5.5. The charge density contours in the different planes (a) 001 plane, 2.20 Å from the origin perpendicular to the z-axis, (b) 010 plane, 1.30 Å from the origin perpendicular to the y-axis and (c) 100 plane, 0.00 Å from the origin perpendicular to the x-axis.

3.4 Optical properties of LiYF₄ crystal

The optical properties of the LiYF₄ crystal are based on the complex dielectric function which represents the linear response of the system to an external electromagnetic field with a small wave vector. In our calculations, the excitonic effect was ignored, while the local field effect was considered. The complex shift in the Kramers-Kronig transformation is 0.1, which is a perfectly acceptable value. Figure 5.6 shows the real and imaginary parts of the complex dielectric functions of the LiYF₄ crystal. The Kramers-Kronig relation is used to extract the real part from the imaginary part of the dielectric function [69]. An important quantity from the real part of the dielectric constant is the zero frequency limit. This value where the energy is equal to zero, i.e. $\varepsilon_1(\omega = 0)$, represents the static dielectric constant. The static dielectric constant of LiYF₄

is 2.03. The static dielectric constant consists of ionic and electronic contributions, and these contributions can be calculated from the dielectric constant and the refractive index. The ionic contributions are found to be very small for this fluoride crystal. On the other hand, the important information from the imaginary part of the dielectric constant are the orbital transitions which can be matched to the DOS (Fig. 5. 4). LiYF₄ has two main peaks located at around 15.00 and 32.12 eV which correspond to the transitions from F 2p to Y 4d, from F 2s and Y 4p to Y 4d, respectively.

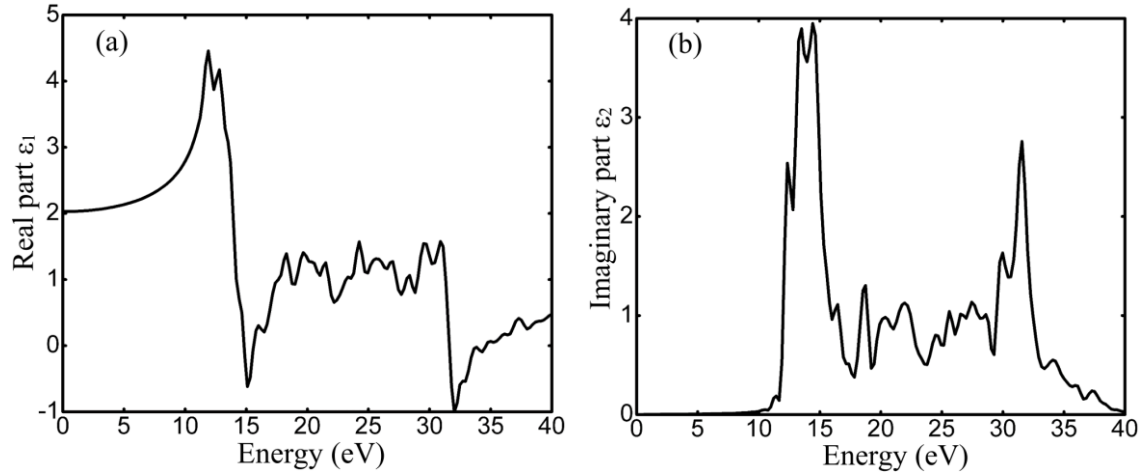
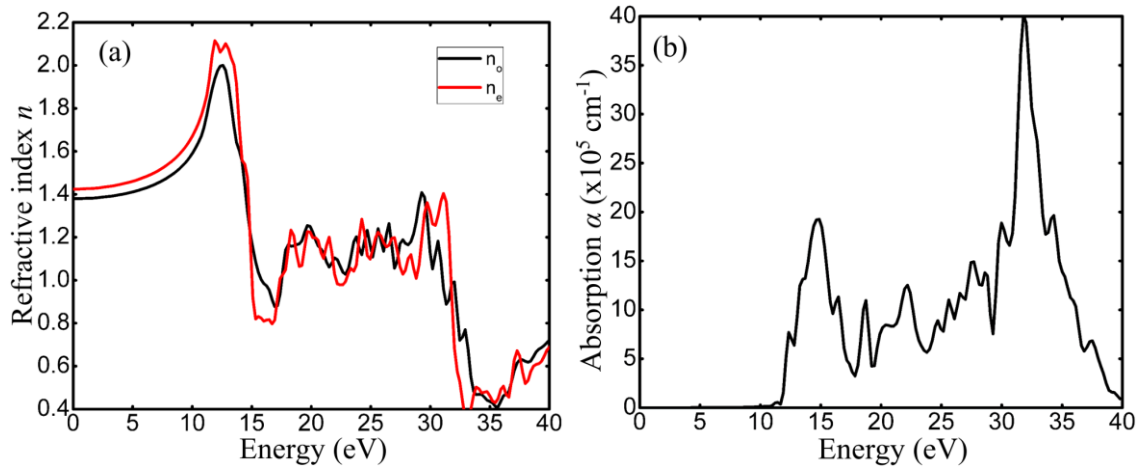


Figure 5. 6: the real part (a) and imaginary parts of dielectric function of the LiYF₄ crystal.

Based on the real and imaginary parts of dielectric function, the optical properties of LiYF₄ crystal such as the refractive index, absorption coefficient, transmittance and reflectivity are calculated and shown in **Fig. 5. 7**. Since LiYF₄ is a birefringent crystal, its refractive index has similar ordinary (n_o) and extra-ordinary (n_e) components. The calculated refractive indices confirm

that YLiF_4 is a positive birefringent crystal where the extra-ordinary refractive index n_e is greater than the ordinary refractive index n_o . The maximum refractive indices are 2.00 and 2.12 for ordinary and extra-ordinary components, respectively. These occur at 11.89 eV. The ordinary and extra-ordinary refractive indices become constant at 1.38 and 1.42, respectively, for wavelengths longer than 400 nm. Our calculations differ by around 3.13 % compared with the experimental refractive index for wavelengths ranging from 225 to 2600 nm (0.48 to 5.51 eV) [97]. The difference could be due to the temperature of the sample during the experiment as the refractive index decreases significantly with temperature [98]. Our calculations are done at 0 K, while the experiments were done at liquid nitrogen temperature (77 K) [97]. LiYF_4 has an absorption band in the VUV region from 100 to 200 nm. We will perform future experiments to confirm these absorption bands. LiYF_4 is highly transparent down to the VUV region with an absorption edge around 121 nm.



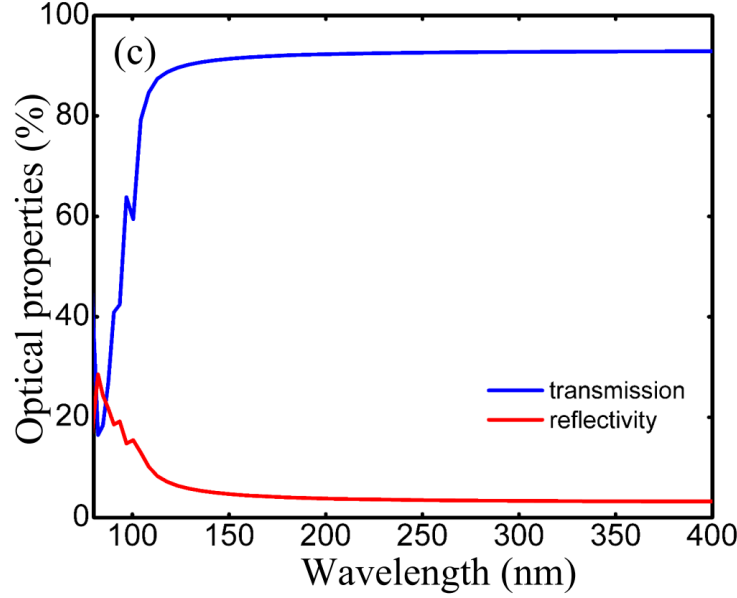


Figure 5. 7: the optical properties such as refractive index (a), absorption coefficient (b), transmission (red) and reflectivity (blue) (c) of the LiYF₄ crystal

In high energy region, the group velocity of the wave packet passing through the material increases than the velocity of light in free space ($v_g > c$ or v_g is negative). Hence, the material shows superluminal behavior.

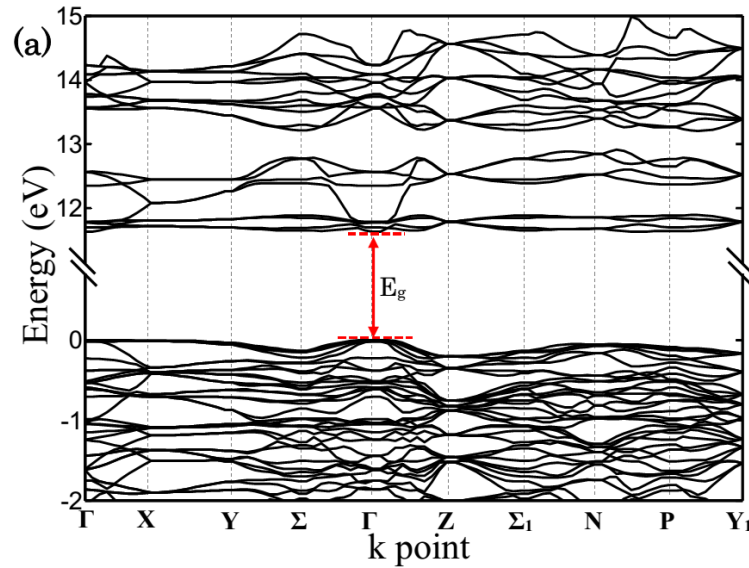
4. Uniform volume compression

Similarity with LiCAF crystal, we investigate the effects of high pressure on the electronic band structure and optical properties of LiYF crystal by uniform compression of the Pulay stress. Originally, LiYF₄‘s band gap is direct and it is very high potential material for VUV laser emission as well as light-emitting diode by doping with p or n type of semiconductor. The

dependence of the crystal volume and band gap energy on the uniaxial compression of this fluoride crystal is also investigated.

4.1 Band structure of LiYF_4 crystal at high pressure

The simulated band structures of the LiYF_4 crystal at different pressures along the symmetry lines of the first Brillouin zone are also shown in Fig. 9.. The band gap of LiYF_4 increases from 11.09 eV at equilibrium to 11.63, 11.86, and 11.86 eV when a pressure of 10, 30, and 50 GPa, respectively, is applied to the crystal. LiYF_4 maintains a direct band gap regardless of the applied pressure as both the valence band maximum and the conduction band minimum are still located at the Γ point. This observation is different from other materials which exhibit band gap transitions from direct to indirect such as LiF or from indirect to direct such as LaAlO_3 [99, 100].



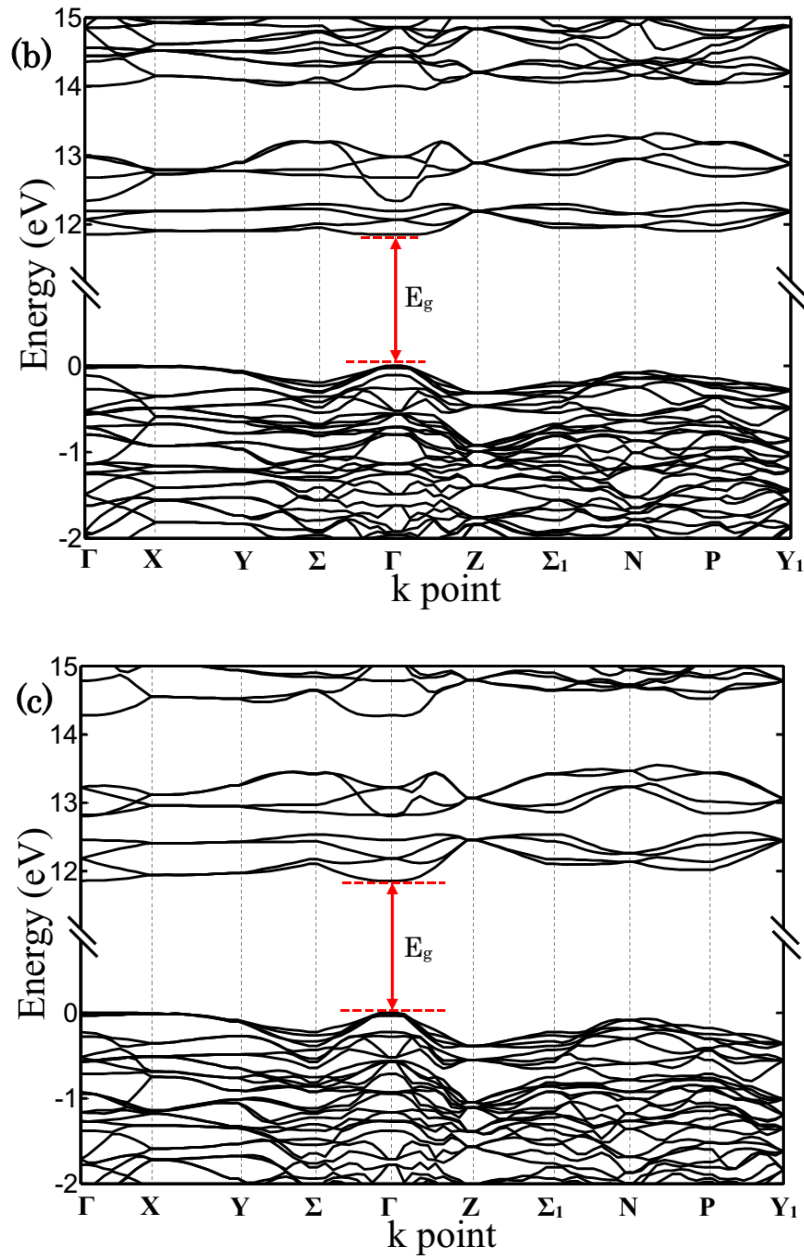


Figure 5.8 The simulated electronic band structure diagrams of LiYF_4 crystal at (a) 10, (b) 30 and (c) 50 GPa. LiYF_4 crystal maintains direct band gap under high pressure up to 50 GPa

4.2 Density of state

To implement the electronic band structures at different pressures, the corresponding total and partial density of states are calculated and shown in figure 5. 9. From total and partial density of states, it shows that the expansions of the bands by pressures.

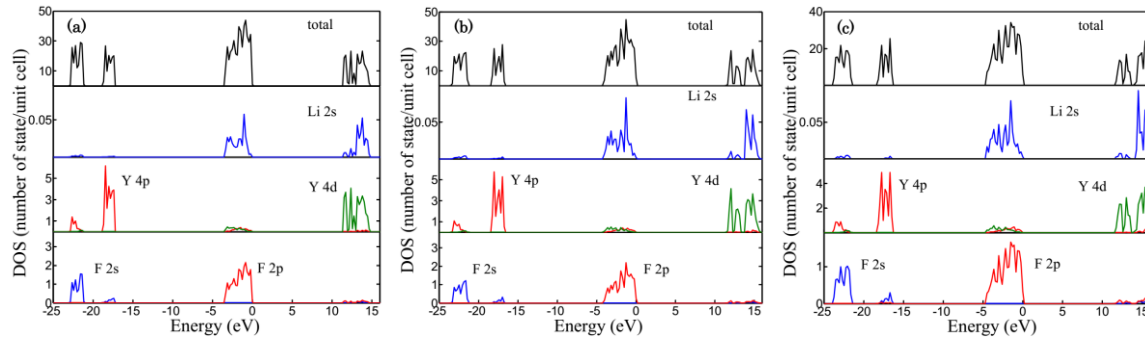


Figure 5. 9: The total and partial density of states of LiYF₄ crystal at (a) 10, (b) 30 and (c) 50 GPa, respectively.

The transition between band gap energy is still from F2p to Y4d orbitals. The increase of valence band width is from 3.46 eV at the zero pressure to 3.56 eV, 4.24 eV and 4.70 eV for 10 GPa, 30 GPa and 50 GPa, respectively. The width of conduction band increases to 3.56 eV, 4.24 eV and 4.92 eV for 10 GPa, 30 GPa and 50 GPa applied pressures.

4.3 Pressure dependence of band gap energy and volume

To identify the effect of high pressure on the band gap energy, the dependence of the crystal volume and band gap energy on the pressure applied uniformly on the crystal is investigated. The calculated pressure is in the range of 0 to 50 GPa with step of 5 GPa. At each applied pressure, the band gap,

optimized volume and lattice constants are calculated and shown in figure 5. 10. The crystal volume decreases with increasing pressure and it is 211.95 \AA^3 (compressed by 25.67 %) at the pressure of 50 GPa. The lattice constants are compressed 10.98 % for a axis and 6.20 % for c axis.

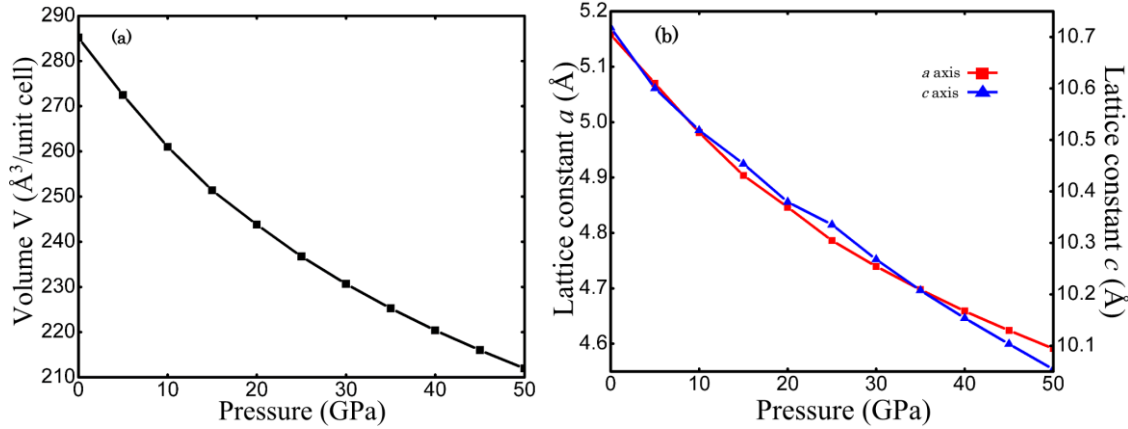


Fig. 5. 10: (a) Optimized crystal volume and (b) lattice constants of the LiYF_4 crystal at different pressures. The crystal volume and lattice constants decreases monotonically since the pressures are applied through uniform volume compression.

The band gap of LiYF_4 gradually increases but then decreases after about 45 GPa. LiYF_4 reaches to the maximum band gap of 11.87 eV at 45 GPa. And then, the band gap energy is slowly decreased by higher pressure application. At the pressure of 50 GPa, LiYF_4 still has a direct band gap of 11.86 eV. In the range of pressure from 0 to 17 GPa, our calculated compressions of volume and lattice constants are good agreement with theoretical and experimental results which is done by X-ray diffraction [6-7].

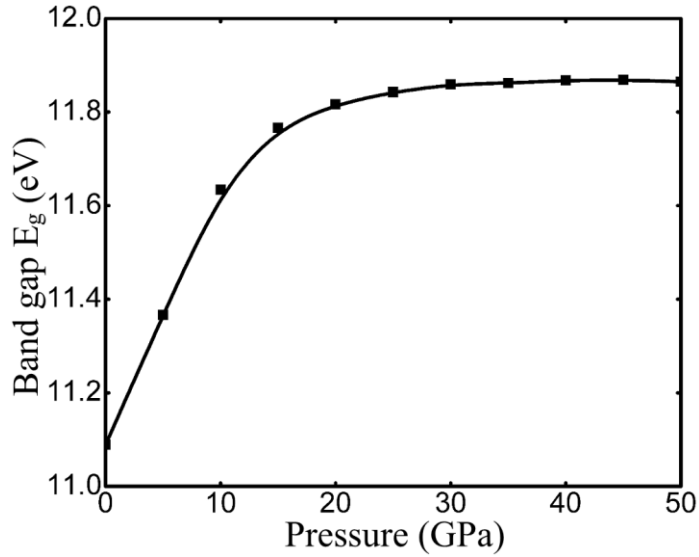


Fig. 5. 11: Band gap energy of the LiYF_4 crystal at different pressures. LiYF_4 has a band gap energy which gradually increases up to 30 GPa and stays almost the same up to 50 GPa.

4.4 Optical properties

Figure 5. 12 shows the real and imaginary parts of complex dielectric function of LiYF_4 crystal at different pressure of 0-50 GPa. For both real and imaginary parts, the first peak of spectra are shifted to higher energy level with increasing of intensities. The static dielectric constant increases to 2.28 and the first peak shifts to 14.01 eV at the 50 GPa. The imaginary part of dielectric function is related to density of state and it was explained in the equilibrium part by orbital transitions. At we mentioned before, by applying high pressure, the valence and conduction bands are expanded, this leads the wider spectra of optical properties.

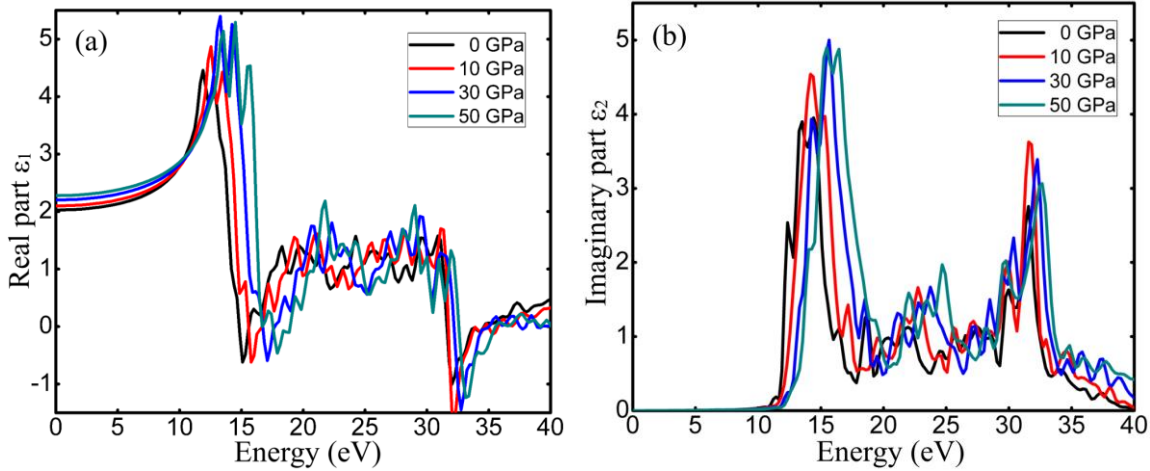


Figure 5.12: the real part (a) and imaginary parts of dielectric function of the LiYF₄ crystal at different pressure.

Similarity with dielectric function, there is a blue-shift for refractive index and absorption coefficient by pressure application.

The refractive index and absorption coefficient of LiYF₄ crystal at the different pressure are shown in figure 5.13. Because of similarity of extra-ordinary and ordinary components of refractive index, the figure 5.13 (a) only shows the extra-ordinary component of refractive index while figure 5.13 (b) shows the absorption spectrum of LiYF crystal. The constant refractive index increases to 1.51 at the pressure of 50 GPa from 1.42 at 0 GPa. The maximum refractive index is 2.36 at 15.48 eV for 50 GPa. The absorption coefficient of LiYF₄ crystal increases from $19.20 \times 10^5 \text{ cm}^{-1}$ at equilibrium to $22.87 \times 10^5 \text{ cm}^{-1}$ at 50 GPa while the location of peak is shifted from 13.72 eV to 15.48 eV.

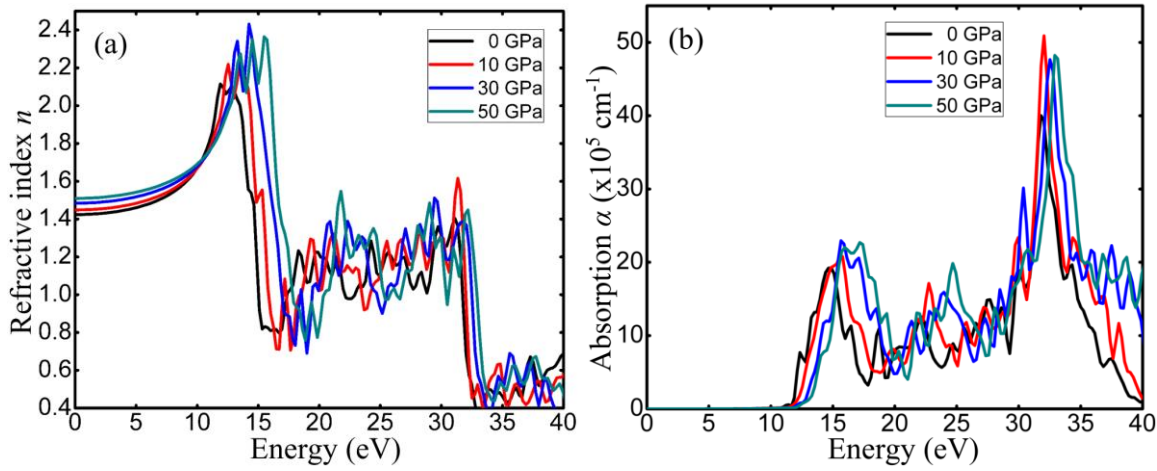


Figure 5. 13: The refractive index (a) and absorption coefficient (b) of the LiYF₄ crystal at different pressure.

The transmission spectrum of LiYF₄ crystal is calculated from absorption coefficient and reflectivity at different pressures and shown in figure 12. To compare with previous experimental result, horizontal axis of spectrum was converted to nanometer. The transmission edge is shifted to shorter wavelength when pressure increases. At zero pressure, the transmission edge is 121 nm while it is 111 nm at 50 GPa.

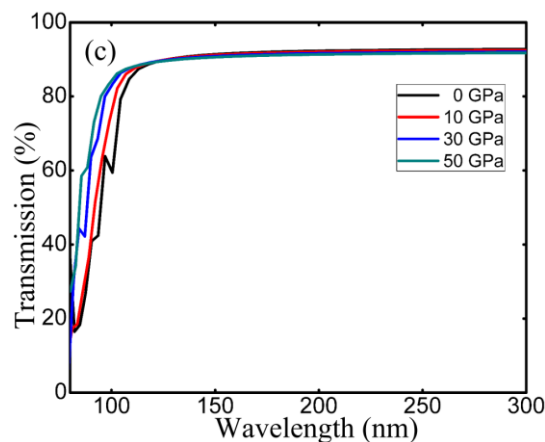


Figure 5. 14: the transmission spectrum of LiYF₄ crystal at different pressure.

5. Pressure dependence of band gap and lattice constants under uniaxial compression

Figure 13 shows the lattice constant compression and band gap energy of the LiYF₄ crystal at different pressures applied through uniaxial compression. Pressures in the range of 0 to 16 GPa are applied separately along the *a*-axis and *c*-axis of the crystal. At 0 GPa, the *a* and *c* lattice constants of LiYF₄ are equal to the equilibrium values of 5.17 and 10.82 Å, respectively. Both lattice constants decrease with increasing pressure. At \sim 14 GPa, the lattice constants compress by 12.56 % for the *a*-axis and by 11.09 % for the *c*-axis. The more compressibility of *a*-axis can be explained by the interaction of ionic inside the LiYF unit cell. As the results of charge density distribution, fluorine atoms have highest charge density comparing with yttrium or lithium. Therefore, the compressibility depends on the interaction between fluorine atoms. The distances between fluorine atoms in *a*-axis and *c*-axis are 3.4 and 2.7 Å, respectively. It leads the *a*-axis is easier compress than *c*-axis for LiYF crystal. The band gap increases monotonically when pressure along the *c*-axis is increased from 0 to 16 GPa. On the other hand, a maximum band gap energy of 11.19 eV is achieved when 3.41 GPa pressure is applied along the *a*-axis. The band gap energy starts to decrease when pressures greater than 3.41 GPa are applied along the *a*-axis. Applying pressure on the crystal along its *c*-axis generally results to a higher band gap. It is therefore more efficient to compress

along the c-axis rather than the a-axis in order to increase the band gap through uniaxial compression.

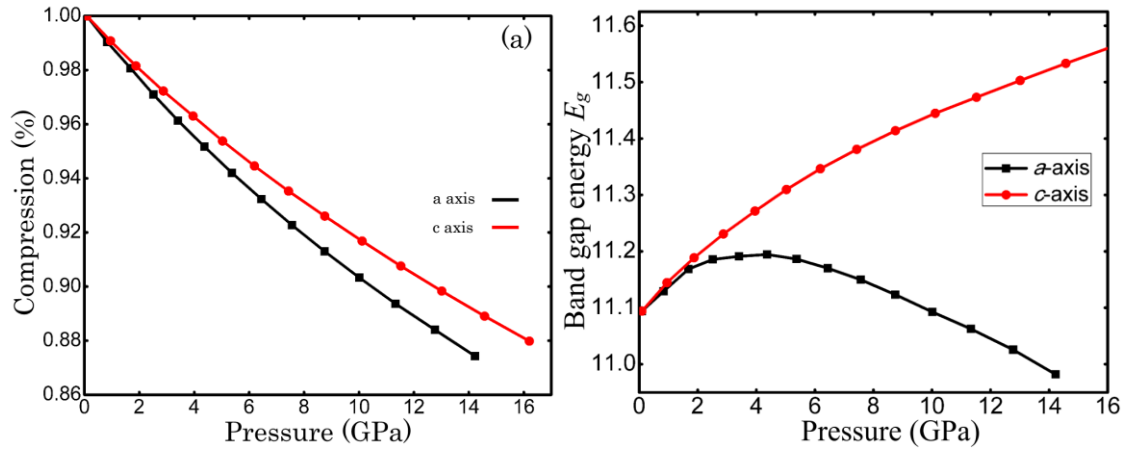


Fig. 5 15 Simulated (a) lattice constant compression and (b) band gap energy of the LiYF₄ crystal at different pressures applied through uniaxial compression.

6. Conclusions

The electronic band structure and optical properties of a perfect LiYF₄ crystal were calculated based on DFT using PBE0 hybrid functional. Our calculations identified the properties of this fluoride crystal at different pressures. At equilibrium (0 GPa), LiYF₄ was found to have a 289.31-Å³ crystal volume and 75.04-GPa bulk modulus, which are all close to the reported experimental values. LiYF₄ was also determined to have a 11.09-eV direct band gap originating from the F 2p to Y 4d transition. Using a better approximation compared to previous reports, we investigated the band gap energy, refractive index, absorption coefficient, and optical transmission of

LiYF_4 at different pressures applied through uniform volume compression. LiYF_4 's band gap energy increased with pressure without any transition from direct to indirect. At 50 GPa, LiYF_4 had a band gap of 11.86 eV with both the valence band maximum and conduction band minimum still located at the Γ point. The absorption band and absorption edge were likewise blue-shifted as the applied pressure increased. The absorption edge shifted from 121 to 111 nm when pressure is increased from equilibrium to 50 GPa. LiYF_4 can be a very good VUV laser host material owing to its wide and direct band gap as well as its controllable absorption spectra through crystal lattice compression. Our findings featured the change in the electronic behavior and optical properties of this fluoride material with pressure. Experimental investigations based on the present results are expected in the near future. This investigation provides helpful insights toward the development of a solid-state and compact VUV light source based on LiYF_4 . High pressure compression can also be applied to other fluoride crystals to improve their properties toward VUV applications.

Chapter 6

Summary and conclusions

The hybrid functional employing an amount of exact exchange is one of most powerful methods to calculate accurate band gap energy. With different materials, the percentage of exact exchanges are different. Firstly, various amounts of exact exchange were initially tested, we estimated that values for LiCAF and LiYF are 35 % and 25 %, respectively which yielded a band gap energy close to the experimental values. LiCAF was found to have indirect band gap of 12.23 eV from the transition between F 2p of valence band maximum and Al 3s of the conduction band minimum. On the other hand, LiYF was found to have direct band gap of 11.09 eV originating from F 2p to Y 4d transition. With wide band gap, both LiCAF and LiYF are potential candidates for VUV laser host materials and optical devices.

By our electronic band structures and density of states, it is helpful to explain some physical phenomena that is experimentally difficult to explain such as the solarization effect on the Ce:LiCAF and Ce:LiSAF crystals or the

absorption peak of LiCAF crystal at around 131 nm is not contamination absorption. Moreover, by knowing the transition between band gap, modification band gap energy is more easier by doping or impurities.

To be best of our knowledge, the optical properties such as refractive index, absorption coefficient or transmission of LiCaAlF and LiYF perfect crystals were calculated for the first time. The GW (Green's function and the screened Coulomb interaction) routine is performed to calculate the optical properties of both fluorides in the equilibrium and high pressure conditions. In this performance, the excitonic effect is considered. These results were compared with experimental observations. Both LiCAF and LiYF are positive birefringent crystals where extra-ordinary refractive index is greater than the ordinary refractive index. The calculated transmission of LiCAF is very good agreement with experiment while transmission of LiYF is firstly calculated at the VUV region where experiment is not achieved. The transmission edges of these fluoride compounds are 112 nm and 121 nm respectively.

For the first time, band gap energies of LiCaAlF₆ and LiYF₄ crystals were also modified by high pressure application through uniform volume and uniaxial compression. We predict that, through uniform volume compression, LiCAF's band gap shifts from indirect to direct at 110.10 GPa and picosecond time scales, arising from the energetic swap of the Al 3s and Ca 4s orbitals. For LiYF crystal, it is original and maintains the direct band gap in the range 0 – 50 GPa of pressure. Wide direct band gap of fluoride materials is not only used

for light emitting diodes but also hopefully laser emission in the VUV region. The absorption bands and absorption edges were likewise blue-shifted as the applied pressure increased.

The investigations of band gap energy under uniaxial compression show that in increasing the band gap of the both fluoride compounds, working along the c-axis is more efficient than working along the a-axis because of band gap energy and compressibility. This result for LiCAF crystal was confirmed by experimental laser-shock compression in chapter 4. Based on success of very first experiment, we suggest the high pressure laser-shock with very short time scale as well as diamond anvil for uniform volume and uniaxial compression in the near future. Our finding featured the change in the electronic behavior and optical properties of these fluoride materials with pressure. More experimental investigations based on the present results are expected to development of a solid-state and compact VUV light sources. Future theoretical and experimental research will probe the effects of pressure on other fluoride compounds in order to gauge whether the electronic properties of these crystals can also be tuned to improve their efficacy in VUV applications.

References

1. M. Sakai, T. Kozeki, H. Murakami, M. Hosomizu, R. Yoshioka, Y. Suzuki, S. Ono, N. Sarukura, H. Sato, and T. Fukuda, “Vacuum-ultraviolet, real time imaging system utilizing LiCaAlF₆ optics” Lasers and Electro-Optics (CLEO) CTHR6 (2003).
2. M. Sakai, Z. Liu, H. Ohtake, N. Sarukura, Y. Segawa, T. Oba, K. Shimamura, S. L. Baldochi, K. Nakano, N. Mujilatu, and T. Fukuda, “LiCAF crystal as a new vacuum ultraviolet optical material with transmission down to 112 nm” Lasers and Electro-Optics (CLEO’99) 497 (1999).
3. K. Shimamura, S. L. Baldochi, I. M. Ranieri, H. Sato, T. Fujita, V. L. Mazzocchi, C. B.R. Parente, C. O. Paiva-Santos, C. V. Santilli, N. Sarukura, and T. Fukuda, “Crystal growth of Ce-doped and undoped LiCaAlF₆ by the Czochralski technique under CF₄ atmosphere” Journal of Crystal Growth **223** 383 (2001).
4. Q. Fang, H. Chen, F. Xu, S. Wang, Z. Liang, and C. Jiang, “Bridgman growth of LiYF₄ single crystal in nonvacuum atmosphere” Chinese Optics Letters **8** 1071 (2010).
5. K. Yamanoi, R. Nishi, K. Takeda, Y. Shinzato, M. Tsuboi, M. V. Luong, T. Nakazato, T. Shimizu, N. Sarukura, M. C. Raduban, M. H. Pham, H. D. Nguyen, S. Kurosawa, Y. Yokota, A. Yoshikawa, T. Togashi, M. Nagasono

- and T. Ishikawa, “Perovskite fluoride crystals as light emitting materials in vacuum ultraviolet region”, *Optical Materials* **36** 769–772 (2014).
6. A. Grzechnik, K. Syassen, I. Loa, M. Hanfland and J. Y. Gesland, “Scheelite to fergusonite phase transition in YLiF_4 at high pressures” *Physical Review B* **65** 104102 (2002).
 7. J. L. Solano, P. R. Hernandez, A. Munoz and F. J. Manjon, “Theoretical study of the scheelite-to-fergusonite phase transition in YLiF_4 under pressure” *Journal of Physical Chemistry of Solids* **67** 2077-2082 (2006).
 8. J. Yin, Q. Zhang, T. Liu, X. Guo, M. Song, X. Wang, and H. Zhang, “Ab initio study electronic structures of LiYF_4 crystal containing interstitial oxygen atoms” *Nuclear Instruments and Methods in Physics Research B* **267** 74 (2009).
 9. J. Yin, Y. Hang, L. Zhang, C. Zhao, J. Xiong, and P. Hu, “Origin of the 330 nm absorption band and effect of doping Yb in LiYF_4 crystals” *Journal of Luminescence* **130** 1338 (2010).
 10. M. H. Du, D.J. Singh, “Electronic structure, small polaron, and F center in LiCaAlF_6 ” *Journal of Applied Physics* **112** 123516 (2012).
 11. W. Y. Ching and Y. N. Xu, “Comparative study of the electronic structure of two laser crystals: BeAl_2O_4 and LiYF_4 ” *Physical Review B* **63** 115101 (2001).
 12. N. Shiran, A. Gekhtin, S. Neicheva, M. Weber, S. Derenzo, M. Kirm, M. True, I. Shpinkov, D. Spassky, K. Shimamura, N. Ichinose “Energy transfer in

- pure and Ce-doped LiCaAlF₆ and LiSrAlF₆ crystals”, Nuclear Instruments and Methods in Physics Research A **537** 266-270 (2005).
13. A. Bensalah, K. Shimamura, K. Nakano, T. Fujita, T. Fukuda, “Growth and characterization of LiSrGaF₆ single crystal” Journal of Crystal Growth **231** 143-147 (2001).
 14. W. Viebahn “Untersuchungen an quaternaren Flouriden LiMe“Me”F₆ Die Struktur von LiCaAlF₆”, Z. anorg. allg. Chem. **386** 335 (1971).
 15. S. A. Payne, L. L. Chase, H. W. Newkirk, L. K. Smith, and W. F. Krupke, “LiCaAlF₆ : Cr³⁺ : A Promising New Solid-state Laser Material” IEEE Journal of Quantum Electronics **24** 2243 (1988).
 16. C. D. Marshall, J. A. Speth, S. A. Payne, and W. F. Krupke, “Ultraviolet laser emission properties of Ce³⁺-doped LiSrAlF₆ and LiCaAlF₆ ” Journal of the Optical Society of America B **11** 2054 (1994).
 17. N. Sarukura, Z. Liu, H. Otake, Y. Segawa, M. A. Dubinskii, V. V. Semashko, A. K. Naumov, S. L. Korableva, and R. Yu. Abdulsabirov, “Ultraviolet short pulses from an all-solid-state Ce:LiCAF master-oscillator–power-amplifier system”, Optics Letters **22** 994-996 (1997).
 18. Z. Liu, S. Izumida, S. Ono, H. Otake, N. Sarukura, K. Shimamura, N. Mujilatu, S. L. Baldochi, and T. Fukuda, “Czochralski-grown large Ce:LiCAF crystal for efficient UV laser with output up to 60-mJ”, Lasers and Electro-Optics **3** 684 (1999).
 19. M. H. Pham, M. M. Cadatal, T. Tatsumi, A. Saiki, Y. Furukawa, T.

- Nakazato, E. Estacio, N. Sarukura, T. Suyama, K. Fukuda, K. J. Kim, A. Yoshikawa, and F. Saito, “Laser Quality $\text{Ce}^{3+}:\text{LiCaAlF}_6$ Grown by Micro-Pulling-Down Method” Japanese Journal of Applied Physics **47** 5605 (2008).
20. M.V. Luong, M. C. Raduban, M. J. F. Empizo, R. Arita, Y. Minami, T. Shimizu, N. Sarukura, H. Azechi, M. H. Pham, H. D. Nguyen, and Y. Kawazoe, “Comparison of the electronic band structures of LiCaAlF_6 and LiSrAlF_6 ultraviolet laser host media from ab initio calculations” Japanese Journal of Applied Physics **54** 122602 (2015).
21. T. Shimizu, M. M. Cadatal, K. Yamanoi, S. Takatori, M. Kouno, M. Pham, E. Estacio, T. Nakazato, N. Sarukura, N. Kawaguchi, K. Fukuda, T. Suyama, T. Yanagida, Y. Yokota, A. Yoshikawa, and F. Saito, “Er:LiCAF as Potential Vacuum Ultraviolet Laser Material at 163 nm” IEEE Transactions on Nuclear Science **57** 1204, (2010).
22. A. Yoshikawa, T. Yanagida, Y. Yokota, A. Yamaji, Y. Fujimoto, J. Pejchal, V. I. Chani, N. Kawaguchi, S. Ishizu, K. Fukuda, T. Suyama, and M. Nikl, “Crystal growth and VUV luminescence properties of Er^{3+} - and Tm^{3+} -doped LiCaAlF_6 for detectors” Optical Materials **32** 845 (2010).
23. E. Sarantopoulou, Z. Kollia, and A.C. Cefalas, “ $\text{LiCaAlF}_6:\text{Nd}^{3+}$ crystal as optical material for 157 nm photolithography” Optics Communications **177** 377 (2000).
24. Y. Minami, R. Arita, M. C. Raduban, M. H. Pham, M. J. F. Empizo, M. V.

- Luong, T. Hori, M. Takabatake, K. Fukuda, K. Mori, K. Yamanoi, T. Shimizu, N. Sarukura, K. Fukuda, N. Kawaguchi, Y. Yokota, and A. Yoshikawa, “Temperature-dependent evaluation of Nd:LiCAF optical properties as potential vacuum ultraviolet laser material” *Optical Materials* **58** 5 (2016).
25. R. E. Thomas, L.A. Harris, G. F Weaver, H. A. Friedman, H. Insley and H. A. Yakel. “Phase equilibria in the system LiF-YF₃” *Journal of Physical Chemistry* **65** 1096 (1961).
26. Z. Liu, K. Shimamura, K. Nakano, Na Mujilatu, T. Fukuda, T. Kozeki, H. Otake, and N. Sarukura, “Direct Generation of 27-mJ, 309-nm Pulses from a Ce³⁺:LiLuF₄ Oscillator Using a Large-Size Ce³⁺:LiLuF₄ Crystal” *Japanese Journal of Applied Physics* **39** L88 (2000).
27. J. Ehrlich, P. F. Moulton, and R. M. Jr. Osgood, “Ultraviolet solid-state Ce:YLF laser at 325 nm” *Optics Letters* **4** 184 (1979).
28. K. Yamanoi, Y. Minami, R. Nishi, Y. Shinzato, M. Tsuboi, M. V. Luong, T. Nakazato, T. Shimizu, N. Sarukura, M. C. Raduban, M. H. Pham, H. D. Nguyen, Y. Yokota, A. Yoshikawa, M. Nagasono, and T. Ishikawa, “VUV fluorescence from Nd³⁺:LuLiF₄ by two photon excitation using femtosecond laser”, *Optical Materials* **35** 2030 (2013).
29. P. W. Dooley, J. Thøgersen, J. D. Gil, H. K. Haugen and R. L. Brooks, “Studies of two-photon excitation and vacuum ultraviolet fluorescence in Nd:YLF” *Optics Communications* **183** 451–459 (2000).

30. S. Froyen, D. M. Wood, and A. Zunger, “New optical transitions in strained Si-Ge superlattices” *Physical Review B* **36** 4547 (1987).
31. A. Sajid, G. Murtaza, and A. H. Reshak, “Shift of band gap from direct to indirect and optical response of LiF under pressure” *Modern Physics Letters B* **27** 1350061 (2013).
32. P. A. M. Dirac, *Quantum Mechanics* (Oxford U.P., London, 1958)
33. Eric J. Heller, “Time-dependent approach to semiclassical dynamics”, *The Journal of Chemical Physics* **62** 1544 (1975).
34. P. J. Redmond, “Solution of the Klein-Gordon and Dirac Equations for a Particle with a Plane Electromagnetic Wave and a Parallel Magnetic Field”, *Journal of Mathematical Physics* **6** 1163 (1965).
35. Robert G. Parr, “Density Functional Theory”, *Chapter Electron Distributions and the Chemical Bond* pp 95-100 Springer (1982).
36. R. Car and M. Parrinello, “Unified Approach for Molecular Dynamics and Density-Functional Theory”, *Physical Review Letters* **55** 2471 (1985).
37. Erich Runge and E. K. U. Gross, “Density-Functional Theory for Time-Dependent Systems”, *Physical Review Letters* **52** 997 (1984).
38. Walter Kohn, Yigal Meir, and Dmitrii E. Makarov, “van der Waals Energies in Density Functional Theory”, *Physical Review Letters* **80** 4153 (1998).
39. Walter Kohn and Ann E. Mattsson, “Edge Electron Gas”, *Physical Review Letters* **81** 3487 (1998).

40. W. Kohn, A. D. Becke, and R. G. Parr, “Density Functional Theory of Electronic Structure”, *Journal of Physical Chemistry* **100** 12974 (1996).
41. W. Kohn, “Nobel Lecture: Electronic structure of matter—wave functions and density functionals”, *Reviews of Modern Physics* **71** 1253 (1999).
42. G. Vignale, M. Rasolt, D.J.W. Geldart, “Magnetic Fields and Density Functional Theory”, *Advances in Quantum Chemistry* **21** 235–253 (1990).
43. Mark S. Hybertsen, E. B. Stechel, M. Schluter, and D. R. Jennison, “Renormalization from density-functional theory to strong-coupling models for electronic states in Cu-O materials”, *Physical Review Letters* **41** 11068 (1990).
44. A. Svane and O. Gunnarsson, “Transition-metal oxides in the self-interaction-corrected density-functional formalism”, *Physical Review Letters* **65** 1148 (1990).
45. W. Kohn and L. J. Sham, “Self-Consistent Equations Including Exchange and Correlation Effects” *Physical Review Letters* **140**, 1133 (1965).
46. J. P. Perdew, “Accurate Density Functional for the Energy: Real-Space Cutoff of the Gradient Expansion for the Exchange Hole” *Physical Review Letters* **55** 1665 (1985).
47. J. P. Perdew and Y. Wang, “Accurate and simple analytic representation of the electron-gas correlation energy” *Physical Review B* **45** 13244 (1992).

48. J. P. Perdew and Y. Wang, "Accurate and simple density functional for the electronic exchange energy: Generalized gradient approximation" *Physical Review B* **33** 8800 (1986).
49. A. D. Becke, "Density-functional exchange-energy approximation with correct asymptotic behavior" *Physical Review A* **38** 3098 (1988).
50. C. Lee, W. Yang, and R. G. Parr, "Development of the Colle-Salvetti correlation-energy formula into a functional of the electron density" *Physical Review B* **37** 785 (1988).
51. B. G. Johnson, P. M. W. Gill, and J. A. Pople, "The performance of a family of density functional methods" *Journal of Chemical Physics* **98** 5612 (1993).
52. J. P. Perdew, J. A. Chevary, S. H. Vosko, K. A. Jackson, M. R. Pederson, D. J. Sigh, and C. Fiolhais, "Atoms, molecules, solids, and surfaces: Applications of the generalized gradient approximation for exchange and correlation" *Physical Review B* **46** 6671 (1992).
53. C. Sosa and C. Lee, "Density functional description of transition structures using nonlocal corrections. Silylene insertion reactions into the hydrogen molecule" *Journal of Chemical Physics* **98** 8004 (1993).
54. P. Bagbo, O. Jepsen, O. Gunnarsson, "Ground-state properties of third-row elements with nonlocal density functionals" *Physical Review B* **40** 1997 (1989).

55. C. Lee, D. Vanderbilt, K. Laasonen, R. Car, M. Parrinello, “Ab initio studies on the structural and dynamical properties of ice” *Physical Review B* **47** 4863 (1993).
56. R. N. Barnett, U. Landman, “Born-Oppenheimer molecular-dynamics simulations of finite systems: Structure and dynamics of (H₂O)₂” *Physical Review B* **48** 2081 (1993).
57. J. P. Perdew and K. Burke, “Comparison Shopping for a Gradient-Corrected Density Functional” *International Journal of Quantum Chemistry* **57** 309 (1996).
58. Y. H. Kim, I. H. Lee, S. Nagaraja, J. P. Leburton, R. Q. Hood, and R. M. Martin, “Two-dimensional limit of exchange-correlation energy functional approximations” *Physical Review B* **61** 5202 (2000).
59. J. P. Perdew, K. Burke, and M. Ernzerhof, “Generalized Gradient Approximation Made Simple” *Physical Review Letters* **77** 3865 (1996).
60. S. K. Ma and K. A. Brueckner, “Correlation Energy of an Electron Gas with a Slowly Varying High Density” *Physical Review* **165** 18-31 (1968).
61. J. P. Perdew, M. Ernzerhof, and K. Burke, “Rationale for mixing exact exchange with density functional approximations” *Journal of Chemical Physics* **105** 9982 (1996).
62. M. Ernzerhof, J. P. Perdew, and K. Burke, “Coupling-constant dependence of atomization energies” *International Journal of Quantum Chemistry* **64** 285 (1997).

63. C. Adamo and V. Barone, “Toward reliable density functional methods without adjustable parameters: The PBE0 model” *Journal of Chemical Physics* **110** 6158 (1999).
64. F. Tran and P. Blaha, “Accurate Band Gaps of Semiconductors and Insulators with a Semilocal Exchange-Correlation Potential”, *Physical Review Letters* **102** 226401 (2009).
65. V. G. Tyuterev, and N. Vast, “Murnaghan’s equation of state for the electronic ground state energy” *Computational Materials Science* **38** 350 (2006).
66. F. Bassani, G. Pastori, and Parravicini, *Electronic States and Optical Transitions in Solids*, Pergamon Press, Oxford (1973).
67. P. Puschnig, and C. Ambrosch-Draxl, “Optical absorption spectra of semiconductors and insulators including electron-hole correlations: An ab initio study within the LAPW method” *Physical Review B* **66** 165105 (2002).
68. S. Sharma, C. Ambrosch-Draxl, M.A. Khan, P. Blaha, and S. Auluck, “Optical properties and band structure of 2H-WSe₂” *Physical Review B* **60** 8610 (1999).
69. V. B. Bobrov, S. A. Trigger, G. J. F. van Heijst and P. P. J. M. Schram, “Kramers-Kronig relations for the dielectric function and the static conductivity of Coulomb systems” *EPL* **90**, 10003 (2010).
70. M. Fox, *Optical properties of Solids*, Oxford University Press, New York (2001).

71. M. Dreesel, G. Gruner, *Electrodynamics of Solid: Optical Properties of Electron in Matter*, Cambridge University Press, UK, (2002).
72. T. Tamm, and M. Peld, “Computational study of cation substitutions in apatites”, *Journal of Solid State Chemistry* **179** 1581–1587 (2006).
73. Y. Ono, K. Nakano, K. Shimamura, T. Fukuda, and T. Kajitani, “Structural study of colquiriite-type fluorides” *Journal of Crystal Growth* **229** 505 (2001).
74. S. Kuze, D. Boulay, N. Ishizawa, N. Kodama, M. Yamaga, B. Henderson, “Structures of LiCaAlF₆ and LiSrAlF₆ at 120 and 300 K by synchrotron X-ray single-crystal diffraction” *J. Solid State Chemistry* **177** 3505 (2004).
75. A. Grzechnik, V. Dmitriev, H. P. Weber, J. Y Gesland and S. V. Smaalen, “LiSrAlF₆ with the LiBaCrF₆-type structure”, *Journal of Physics: Condensed Matter* **16** 3005-3013 (2004).
76. M. V. Luong, M. J. F. Empizo, M. C. Raduban, R. Arita, Y. Minami, T. Shimizu, N. Sarukura, H. Azechi, M. H. Pham, H. D. Nguyen, Y. Kawazoe, K. G. Steenbergen, and P. Schwerdtferger, “First-principles calculations of electronic and optical properties of LiCaAlF₆ and LiSrAlF₆ crystals as VUV to UV solid-state laser materials” *Optical Materials* just accepted (2016).
77. W. Setyawan and S. Curtarolo, “High-throughput electronic band structure calculations: challenges and tools” *Computational Materials Science* **49** 299 (2010).

78. B. W. Woods, S.A. Payne, J.E. Marion, R.S. Hughes, L.E. Davis, "Thermomechanical and thermo-optical properties of the LiCaAlF₆:Cr³⁺ laser material" *Journal of the Optical Society of America B* **8** 970-977 (1991).
79. K. Shimamura, H. Sato, A. Bensalah, H. Machida, N. Sarukura, T. Fukuda, "Growth of LiCaAlF single crystals with an extended diameter and their optical characterizations", *Journal of Alloys and Compounds* **343** 204–210 (2002).
80. R. D. Peterson, A.T. Pham, H.P. Jenssen, A. Cassanho, and V. Castillo, "Thermo-Optical Comparison of LiSAF, LiCAF, and LiSGaF", *Advanced Solid State Lasers OSA Trends in Optics and Photonics* (Optical Society of America) paper TuB6 (1999).
81. K. Shimamura, S.L. Baldochi, N. Mujilatu, K. Nakano, Z. Liu, N. Sarukura, T. Fukuda, "Growth of Ce-doped LiCaAlF₆ and LiSrAlF₆ single crystals by the Czochralski technique under CF₄ atmosphere" *Journal of Crystal Growth* **211** 302-307 (2000).
82. K. I. Schaffers and D. A. Keszler "Structure of LiSrAlF₆", *Acta Crystallographica Section C* **47** 18 (1991).
83. S. Koizumi, K. Watanabe, F. Hasegawa, and H. Kanda, "Ultraviolet emission from a diamond pn junction" *Science* **292** 1899 (2001).
84. J. K. Lawson and S. A. Payne, "Excited-state absorption of Eu²⁺-doped materials" *Physical Review B* **47** 14003 (1993).

85. R. Moncorge, in *Ultraviolet Spectroscopy and UV Lasers*, ed. P. Misra and M. A. Dubinskii (CRC Press, Boca Raton, FL, 2002) Chap. 9
86. N. Sarukura, Z. Liu, S. Izumida, M. A. Dubinskii, R. Y. Abdulsabirov, and S. L. Korableva, “All-Solid-State Tunable Ultraviolet Subnanosecond Laser with Direct Pumping by the Fifth Harmonic of a Nd:YAG laser” *Applied Optics* **37** 6446 (1998).
87. A. J. Bayramian, C. D. Marshall, J. H. Wu, J. A. Speth, S. A. Payne, G. J. Quarles, and V. K. Castillo, “Ce³⁺: LiSrAlF₆ laser performance with antisolarant pump beam”, *Journal of Luminescence* **69** 85-94 (1996).
88. K. Ichiyanagi and K. Nakamura, “Structural Dynamics of Materials under Shock Compression Investigated with Synchrotron Radiation” *Metals*. **6** 17 (2016).
89. J. Hu, K. Ichiyanagi, T. Doki, A. Goto, T. Eda, K. Norimatsu, S. Harada, D. Horiuchi, Y. Kabasawa, S. Hayashi, S. Uozumi, N. Kawai, S. Nozawa, T. Sato, S Adachi, and K. G. Nakamura, “Complex structural dynamics of bismuth under laser-driven compression” *Applied Physics Letters* **103** 161904 (2013).
90. L. Berthe, R. Fabbro, P. Peyre, L. Tollier, and E. Bartnicki, “Shock waves from a water-confined laser-generated plasma” *Journal of Applied Physics* **82** 2826 (1997).
91. J. E. Miller and E. J. Sharp, “Optical Properties and Energy Transfer in LiYF₄: Nd³⁺, Yb³⁺”, *Journal of Applied Physics* **41** 4718 (1970).

92. K. Ogasawara, S. Watanabe, H. Toyoshima, T. Ishii, M.G. Brik, H. Ikeno, and I. Tanaka, “Optical spectra of trivalent lanthanides in LiYF₄ crystal” *Journal of Solid State Chemistry* **178** 412 (2005).
93. E. Garcia and R. R. Ryan, “Structure of the Laser Host Material LiYF_{4”} *Acta Crystallographica Section C* **49** 2053 (1993).
94. Markus P. Hehlen ; William L. Boncher ; Seth D. Melgaard ; Michael W. Blair ; Robert A. Jackson ; Thomas E. Littleford ; Steven P. Love, “Preparation of high-purity LiF, YF₃, and YbF₃ for laser refrigeration”, *Proc. SPIE 9000, Laser Refrigeration of Solids VII*, 900004 (2014).
95. P. Blanchfield and G. A. Saunders, “The elastic constants and acoustic symmetry of LiYF”, *Journal of Physics C: Solid State Physics* **12** 4673 (1979).
96. S. Li, R. Ahuja and B. Johansson, “Wolframite: the post-fergusonite phase in YLiF_{4”}, *Journal of Physics: Condensed Matter* **16**, S983 (2004).
97. N. P. Barnes and D. J. Gettemy, “Temperature variation of the refractive indices of yttrium lithium fluoride”, *Journal of the Optical Society of America* **70** 1244 (1980).
98. R. M. Waxler and G. W. Cleek, “The Effect of Temperature and Pressure on the Refractive Index of Some Oxide Glasses”, *Journal of Research of the National Bureau of Standards - A. Physics and Chemistry* **77** 755 (1973).

99. A. Sajid, G. Murtaza and A. H. Reshak, "Shift of band gap from direct to indirect and optical response of LiF under pressure" *Modern Physics Letters B* **27** 1350061 (2013).
100. G. Murtaza and I. Ahmad, "Shift of indirect to direct bandgap and optical response of LaAlO₃ under pressure" *Journal of Applied Physics* **111** 123116 (2012).

List of publications

1. Mui Viet Luong, Melvin John F. Empizo, Yuki Minami, Toshihiko Shimizu, Nobuhiko Sarukura, Hiroshi Azechi, Minh Hong Pham, Hung Dai Nguyen, Marilou Cadatal-Raduban, Krista G. Steenbergen, and Peter Schwerdtferger, “*Direct band gap tunability of LiYF₄ crystal by uniaxial and uniform volume compression*”, preparation in progress.
2. Toshihiko Shimizu, Mui Viet Luong, Melvin John F. Empizo, Marilou Cadatal-Raduban, Kohei Yamanoi, Ren Arita, Yuki Minami, Nobuhiko Sarukura, Hiroshi Azechi, Minh Hong Pham, Hung Dai Nguyen, Kouhei Ichiyanagi, Kentaro Fukuda, Yoshiyuki Kawazoe, Krista G. Steenbergen, and Peter Schwerdtferger, “*High pressure band gap modification of LiCaAlF₆*”, *Applied Physics Letters* **110**, 141902 (2017).
3. Mui Viet Luong, Melvin John F. Empizo, Marilou Cadatal-Raduban, Ren Arita, Yuki Minami, Toshihiko Shimizu, Nobuhiko Sarukura, Hiroshi Azechi, Minh Hong Pham, Hung Dai Nguyen, Yoshiyuki Kawazoe, Krista G. Steenbergen, Peter Schwerdtferger, “*First-principles calculations of electronic and optical properties of LiCaAlF₆ and LiSrAlF₆ crystals as VUV to UV solid-state laser materials*”, *Optical Materials* **65**, 15 - 20 (2017).
4. Melvin John F. Empizo, Alexandra B. Santos-Putungan, Kohei Yamanoi, Hernanie T. Salazar Jr., Eloise P. Anguluan, Kazuyuki Mori, Ren Arita, Yuki Minami, Mui Viet Luong, Toshihiko Shimizu, Elmer S. Estacio, Armando S. Somintac, Arnel A. Salvador, Roland V. Sarmago, Tsuguo Fukuda, Nobuhiko

Sarukura “*Structural and optical characterization and scintillator application of hydrothermal-grown ZnO microrods*”, Optical Materials **65**, 82 - 87 (2017).

5. Ren Arita, Melvin John F. Empizo, Yuki Minami, Mui Viet Luong, Taniguchi Takaya, Yamanoi Kohei, Toshihiko Shimizu, Nobuhiko Sarukura, Marilou Cadatal-Raduban, Pham Duong Van, Nguyen Xuan Tu, Pham Hong Minh, “*A high Q-factor, easy-to-use, broadband Ce:LiCAF laser resonator based on total internal reflection*” Communication in Physics **26**, 245 – 249 (2016).
6. Yuki Minami, Ren Arita, Marilou Cadatal-Raduban, Minh Hong Pham, Melvin John Fernandez Empizo, Mui Viet Luong, Tatsuhiro Hori, Masahiro Takabatake, Kazuhito Fukuda, Kazuyuki Mori, Kohei Yamanoi, Toshihiko Shimizu, Nobuhiko Sarukura, Kentaro Fukuda, Noriaki Kawaguchi, Yuui Yokota, Akira Yoshikawa, “*Temperature-dependent evaluation of Nd:LiCAF optical properties as potential vacuum ultraviolet laser material*”, Optical Materials **58** 5-8 (2016).
7. Mui Viet Luong, Marilou Cadatal-Raduban, Melvin John F. Empizo, Ren Arita, Yuki Minami, Toshihiko Shimizu, Nobuhiko Sarukura, Hiroshi Azechi, Minh Hong Pham, Hung Dai Nguyen, and Yoshiyuki Kawazoe, “*Comparison of the electronic band structures of LiCaAlF₆ and LiSrAlF₆ ultraviolet laser host media from ab initio calculations*” Japanese Journal of Applied Physics **54**, 122602 (2015).
8. Melvin John F. Empizo, Kohei Yamanoi, Alexandra B. Santos-Putungan, Ren Arita, Yuki Minami, Mui Viet Luong, Toshihiko Shimizu, Elmer S. Estacio, Armando S. Somintac, Arnel A. Salvador, Roland V. Sarmago, Nobuhiko Sarukura “*Blue-shifted and picosecond amplified UV emission from aqueous chemical grown ZnO microrods*,” Optical Materials **48**, 179 (2015).

9. Ren Arita, Yuki Minami, Marilou Cadatal-Raduban, Minh Hong Pham, Melvin John Fernandez Empizo, Mui Viet Luong, Tatsuhiro Hori, Masahiro Takabatake, Kazuhito Fukuda, Kazuyuki Mori, Kohei Yamanoi, Toshihiko Shimizu, Nobuhiko Sarukura, Kentaro Fukuda, Noriaki Kawaguchi, Yuui Yokota, Akira Yoshikawa
“Significant blue-shift in photoluminescence excitation spectra of Nd³⁺:LaF₃ potential laser medium at low temperature,” Optical Materials **47**, 462 (2015).
10. Melvin John F. Empizo, Kohei Yamanoi, Kazuyuki Mori, Ren Arita, Keisuke Iwano, Masahiro Takabatake, Kazuhito Fukuda, Tatsuhiro Hori, Yuki Minami, Mui Viet Luong, Yuki Abe, Sadaoki Kojima, Yasunobu Arikawa, Toshihiko Shimizu, Nobuhiko Sarukura, Takayoshi Norimatsu, Hiroshi Azechi, Arnel A. Salvador, Roland V. Sarmago, and Tsuguo Fukuda, *“Gamma-ray irradiation effects on the optical properties of bulk ZnO single crystals”*, Applied Physics Express **8**, 061101 (2015)
11. Minh Hong Pham, Marilou Cadatal-Raduban, Mui Viet Luong, Hai Hoang Le, Kohei Yamanoi, Tomoharu Nakazato, Toshihiko Shimizu, Nobuhiko Sarukura, and Hung Dai Nguyen, *“Numerical simulation of ultraviolet picosecond Ce:LiCAF laser emission by optimized resonator transients”* Japanese Journal of Applied Physics **53**, 062701 (2014).
12. Kohei Yamanoi, Ryosuke Nishi, Kohei Takeda, Yuki Shinzato, Mizuki Tsuboi, Mui Viet Luong, Tomoharu Nakazato, Toshihiko Shimizu, Nobuhiko Sarukura, Marilou Cadatal-Raduban, Minh Hong Pham, Hung Dai Nguyen, Shunsuke Kurosawa, Yuui Yokota, Akira Yoshikawa, Tadashi Togashi, Mitsuru Nagasono, Tetsuya Ishikawa, *“Perovskite fluoride crystals as light emitting materials in vacuum ultraviolet region”*, Optical Materials **36**, 769–772 (2014).

13. Mizuki Tsuboi, Kohei Takeda, Tomoharu Nakazato, Masahiro Kono, Kohei Yamanoi, Marilou Cadatal-Raduban, Kohei Sakai, Ryosuke Nishi, Yuki Minami, Mui Viet Luong, Yasunobu Arikawa, Toshihiko Shimizu, Nobuhiko Sarukura, Takayoshi Norimatsu, Mitsuo Nakai, Hiroshi Azechi, Takahiro Murata, Shigeru Fujino, Hideki Yoshida, Akira Yoshikawa, Nakahiro Sato, Hirofumi Kan, and Kei Kamata, “*Electronic States of Trivalent Praseodymium Ion Doped in 20Al(PO₃)₃–80LiF Glass*” Japanese Journal of Applied Physics **52**, 062402 (2013).
14. Kohei Yamanoi, Yuki Minamia, Ryosuke Nishi, Yuki Shinzato, Mizuki Tsuboi, Mui Viet Luong, Tomoharu Nakazato, Toshihiko Shimizu, Nobuhiko Sarukura, Marilou Cadatal-Raduban, Minh Hong Pham, Hung Dai Nguyen, Yuui Yokota, Akira Yoshikawa, Mitsuru Nagasono, Tetsuya Ishikawa, “*VUV fluorescence from Nd³⁺:LuLiF₄ by two photon excitation using femtosecond laser*” Optical Materials **35**, 2030–2033 (2013).

List of attended scientific conferences

1. Nobuhiko Sarukura, MJ Empizo, K Yamanoi, K Mori, K Iwano, Y Minami, MV Luong, T Shimizu, T Norimatsu, H Azechi, A Salvador, RV Sarmago, T Fukuda, “*Gamma-ray irradiation of hydrothermal-grown bulk zinc oxide single crystals*”, 34th SPP Physics Congress, 2016/08/18-21, University of the Philippines Visayas, Iloilo Campus, Philippines.
2. Y. Minami, T. Shimizu, M. J. F. Empizo, K. Yamanoi, K. Mori, R. Arita, M. V. Luong, T. Nakazato, M. Cadatal-Raduban, N. Sarukura, H. Nishimura, H. Azechi, T. Fukuda, M. Maruyama, M. Nishikino and T. Kawachi, “*Development of a fast zinc oxide scintillator for the short wavelength region using soft X-ray laser*”, The 15th International Conference on X-Ray Lasers (ICXRL2016) 2016/05/22-05/27 Nara Kasugano International Forum, Japan.
3. Mui Viet Luong, Marilou Cadatal-Raduban, Melvin John F. Empizo, Ren Arita, Yuki Minami, Toshihiko Shimizu, Nobuhiko Sarukura, Hiroshi Azechi, Minh Hong Pham, Hung Dai Nguyen, and Yoshiyuki Kawazoe, “*Electronic band structures and density of states of LiCaAlF₆ and LiSrAlF₆ as VUV laser host media*”, 7th International Symposium on Optical Materials (IS-OM7) 2016/02/29-03/04, Claude Bernard Lyon 1 University, France.
4. Nobuhiko Sarukura, Melvin John F. Empizo, Kohei Yamanoi, Kazuyuki Mori, Ren Arita, Keisuke Iwano, Masahiro Takabatake, Kazuhito Fukuda, Tatsuhiro Hori, Yuki Minami, Mui Viet Luong, Yuki Abe, Sadaoki Kojima, Yasunobu Arikawa, Toshihiko Shimizu, Takayoshi Norimatsu, Hiroshi Azechi, Arnel A. Salvador,

Roland V. Sarmago, Tsuguo Fukuda, “*Gamma-ray radiation resistance and improved emission lifetimes of hydrothermal-growth bulk ZnO single crystals*”, 7th International Symposium on Optical Materials (IS-OM7) 2016/02/29-03/04, Claude Bernard Lyon 1 University, France.

5. M.V. Luong, K. Yamanoi, R. Nishi, K. Takeda, Y. Shinzato, M. Tsuboi, M.J.F. Empizo, T. Nakazato, T. Shimizu, N. Sarukura, M. Cadatal-Raduban, M.H. Pham, H.D. Nguyen, S Kurosawa, Y. Yokota, A. Yoshikawa, T. Togashi, M. Nagasono, and T. Ishikawa, “*Vacuum ultraviolet (VUV) fluorescence of KMgF₃ and BaLiF₃ crystals for short wavelength devices*”, Conference on Laser and Synchrotron Radiation Combination Experiment (LSC’14), 2014/4/22-24, Yokohama, Japan.
6. Yuki Minami, Kohei Yamanoi, Tatsuhiko Hori, Ryosuke Nishi, Takeda, Shinzato, Mizuki Tsuboi, Mui Viet Luong, Tomoharu Nakazato, Toshihiko Shimizu, Nobuhiko Sarukura, Marilou Cadatal-Raduban, Minh Hong Pham, Hung Dai Nguyen, Shunsuke Kurosawa, Yuui Yokota, Akira Yoshikawa, Tadashi Togashi, Mitsuru Nagasono, and Tetsuya Ishikawa, “*Photoluminescence properties of KMgF₃ and BaLiF₃ crystals excited by extreme ultraviolet free electron laser*”, 12th International Conference on Inorganic Scintillators and their Applications (SCINT 2013), 2013/4/15-19, Shanghai, China.
7. Pham Hong Minh, Kohei Yamanoi, Yuki Minami, Ryosuke Nishi, Yuki Shinzato, Mizuki Tsuboi, Luong Viet Mui, Tomoharu Nakazato, Toshihiko Shimizu, Nobuhiko Sarukura, Marilou Cadatal-Raduban, Yuui Yokota, Akira Yoshikawa, “*Nd³⁺:LuLiF₄ Vacuum-Ultraviolet Fluorescence arising from two-photon absorption of 290nm excitation*”, The 7th International Conference on Photonics and Applications (ICPA-7), 26-29 November, 2012 in Ho Chi Minh, Viet Nam.

8. Pham Hong Minh, Luong Viet Mui, Nguyen Dai Hung, Nobuhiko Sarukura.,, “*Spectral - Dynamics of All Solid - State Ultraviolet Ce: LiCAF Laser Emissions*”, The 7th International Conference on Photonics and Applications (ICPA-7), 26 - 29 November, 2012 in Ho Chi Minh, Viet Nam.
9. Minh Hong Pham, Nguyen Dai Hung, Marilou Cadatal-Raduban, Luong Viet Mui, Kohei Takeda, Kohei Yamanoi, Tomoharu Nakazato, Toshihiko Shimizu, and Nobuhiko Sarukura, “*Diamond-cut Ce:LiCAF Crystal as Prospectively for Side-pumped Amplifier Design for Amplification of Femtosecond Ultraviolet Pulses*”, The 7th Asian Symposium on Intense Laser Science (ASILS7), University of Tokyo, Japan, 8-9, November, 2012.
10. Nguyen Van Hao, Luong Viet Mui, Trinh Dinh Huy, and Nguyen Dai Hung, “*The characteristics in CW and passively Q-switched laser operations of solid-state Nd³⁺-doped lasers end-pumped by CW high power laser diodes (up to 30 W)*”, The 7th Vietnamese Conference on Solid-State and Material Science (SPMS-2011) Ho Chi Minh City, 7-9/11/2011.